

A coarse-grained model of affinity maturation indicates the importance of B-cell receptor avidity in epitope subdominance

Victor Ovchinnikov^{1,*} and Martin Karplus^{1,2,*}

¹Department of Chemistry and Chemical Biology, Harvard University, Cambridge, MA, 02138, USA

²Laboratoire de Chimie Biophysique, ISIS, Université de Strasbourg, 67000 Strasbourg, France

Correspondence*:

Victor Ovchinnikov, 12 Oxford St, Department of Chemistry and Chemical Biology, Cambridge, MA, 02138, USA

ovchinn@fas.harvard.edu or ovchinnv@georgetown.edu

Martin Karplus, 12 Oxford St, Department of Chemistry and Chemical Biology, Cambridge, MA, 02138, USA, marci@tammy.harvard.edu

2 ABSTRACT

3 The elicitation of broadly neutralizing antibodies (bnAbs) is a major goal in the design of vaccines
4 against rapidly-mutating viruses. In the case of influenza, many bnAbs that target conserved
5 epitopes on the stem of the hemagglutinin protein (HA) have been discovered. However, these
6 antibodies are rare, are not boosted well upon reinfection, and often have low neutralization
7 potency, compared to strain-specific antibodies directed to the HA head. Different hypotheses
8 have been proposed to explain this phenomenon. We use a coarse-grained computational model
9 of the germinal center reaction to investigate how B-cell receptor binding valency affects the
10 growth and affinity maturation of competing B-cells. We find that receptors that are unable to
11 bind antigen bivalently, and also those that do not bind antigen cooperatively, have significantly
12 slower rates of growth, memory B-cell production, and, under certain conditions, rates of affinity
13 maturation. The corresponding B-cells are predicted to be outcompeted by B-cells that bind
14 bivalently and cooperatively. We use the model to explore strategies for a universal influenza
15 vaccine, *e.g.*, how to boost the concentrations of the slower growing cross-reactive antibodies
16 directed to the stem. The results suggest that, upon natural reinfections subsequent to vaccination,
17 the protectiveness of such vaccines would erode, possibly requiring regular boosts. Collectively,
18 our results strongly support the importance of bivalent antibody binding in immunodominance,
19 and suggest guidelines for developing a universal influenza vaccine.

20 **Keywords:** germinal center, simulation, influenza, hemagglutinin, vaccination

1 INTRODUCTION

21 Viral respiratory infections remain a high source of morbidity and mortality around the world. Universal
22 vaccines against highly-mutable viruses such as influenza and HIV are therefore highly desirable. However,

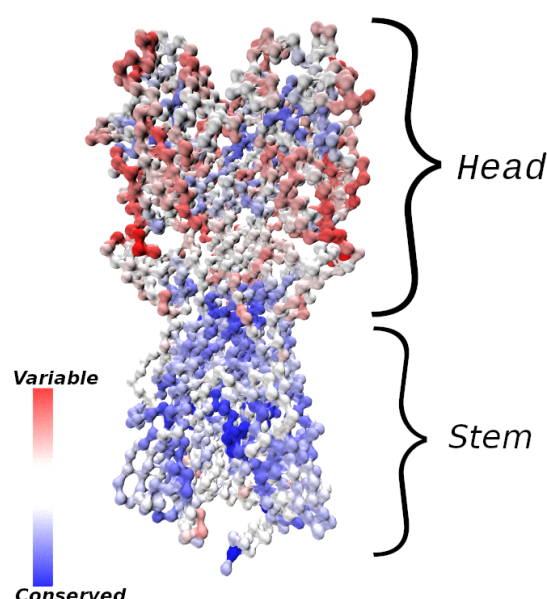


Figure 1. Influenza hemagglutinin (HA) spike protein colored by residue conservation. Sequences of avian, swine and human influenza type A spike proteins **spanning the years 1918–2019 and subtypes 1-18** were downloaded from the NIH influenza research database(3); conservation was computed in MATLAB(4) after clustering the sequences to 97% identity and multiple alignment. The HA structure was taken from PDB entry 3LZG(5), and the image was generated using Visual Molecular Dynamics.(6) Only the C_{α} atoms are shown.

23 their development is complicated by the high antigenic drift of the viral genomes, which stems from
 24 low replicative fidelity of viral nucleic acid polymerases. In the case of influenza, there also exists the
 25 possibility of antigenic ‘shifts’, whereby genome segments from different viral strains are reassorted in a
 26 host co-infected with multiple viruses. Such reassortments can result in pandemic strains against which
 27 preexisting immunity in the affected population is low. For example, the H1N1 1918 influenza pandemic
 28 was likely caused by a reassortment between avian and human influenza strains, the 2009 H1N1 pandemic
 29 was probably caused by a triply reassorted human, avian, and swine strain,(1) and the SARS-CoV2
 30 pandemic is believed to have originated from a bat virus adapted to infect humans and other hosts.(2)

31 Despite the high mutation potential of many viruses, epitopes that are relatively well conserved between
 32 different strains, and antibodies that bind to them, have been discovered. In the case of the influenza
 33 hemagglutinin (HA) protein (see Fig. 1), the majority of conserved epitopes are located on the stem or base
 34 of the HA(7, 8); less frequently, they are found in the HA head, *e.g.*, at the interface between the heads
 35 of HA monomers(9, 10) in a homotrimer, or in the vicinity of the sialic acid receptor(11, 12). There are
 36 different plausible reasons for the increased sequence conservation of these regions, such as (i) maintenance
 37 of function (*e.g.* the sialic acid receptor is required for host cell entry, and properly folded and probably
 38 somewhat rigid HA helices are needed for fusion with the host cell) and (ii) a lack of evolutionary pressure
 39 to drive escape mutants(11); the stem epitopes and the occluded epitope(9) are less accessible to antibodies,
 40 and thus experience less selective pressure than the exposed HA head. Because antibodies (Abs) that bind
 41 conserved epitopes could confer protection against many different viral strains, the elicitation of such
 42 cross-reactive, or broadly-neutralizing Abs (bnAbs) has been a goal of vaccine development.(7) BnAbs
 43 have been isolated from animal and human subjects in response to natural infection or vaccination,(8)
 44 and some have been engineered(13) to have very high breadth, providing simultaneous protection against
 45 phylogenetically distant group I and II HAs.(14, 15, 13) **We note, however, that strong sequence or**

structural conservation of epitopes shared by different antigens is not an absolute requirement for targeting by bnAbs, as many polyreactive and self-reactive bnAbs have been discovered that are able to bind divergent ligands through structural flexibility.(16, 17)

Unfortunately, bnAbs tend to be rare and are not well boosted in infections(15, 18, 19, 20). Further, most of them have lower neutralization potency, compared to strain-specific Abs. However, bnAbs have different mechanisms of protection, *e.g.* labeling infected cells for destruction by Ab-directed cytotoxicity (ADCC), or inhibiting membrane fusion after phagocytosis by the host cell,(7) rather than blockage of viral binding to cells, so that direct comparisons between different Abs are not always informative. Many bnAbs have been shown to provide heterosubtypic protection in passive immunization studies,(8) indicating that their elicitation by a vaccine could provide broad immunity. In the case of influenza, titers of stem-directed Abs have been shown to increase with age, correlating inversely with incidence of symptomatic infection.(21)

The antigenic epitopes targeted by rare bnAbs are labeled immunosubdominant, because they usually are not the primary targets of immune responses. Since durable vaccine responses against highly-mutable pathogens will need to overcome immunodominance, *i.e.* to focus on conserved subdominant epitopes, various possible causes for subdominance have been considered. They include (i) epitope autoreactivity,(12) (ii) low frequency of **germline** precursor antibodies able to bind the epitopes in question,(22) **which is related to the idea of “holes” in the human antibody repertoire, exploited by HIV to protect its conserved regions(23)**, (iii) epitope shielding by glycans,(10) (iv) preexisting immune memory,(22, 20) (v) poor steric accessibility of epitopes(24), (vi) inability to recruit sufficient T-cell help in germinal centers (GCs) due to a lack of compatible MHCII (major histocompatibility complex of type 2) epitopes,(19) and (vii) entropic dominance of distracting epitopes.(25, 24, 26) Although multiple effects are likely to contribute, it is of interest to identify the most important ones. In the context of influenza HA, especially in regard to the stem and the occluded interfacial epitope of Watanabe et al. (9), low steric accessibility appears to be a particularly important factor.

Andrews et al. (22) found that some stem-directed Abs bound virus particles with an affinity that was an order of magnitude lower than that for recombinant HA, which was interpreted in terms of reduced accessibility of stem epitopes of whole virions. **Harris et al. (27) used cryo-electron tomography (cryo-ET) to estimate the average spacing between HA spikes on influenza virions to be 14nm, which appears to be compatible with bivalent binding of antibodies to the HA stem, based on the docking of an unrelated mouse IgG antibody.(27) However, although the study demonstrated that stem epitopes are accessible to antibodies, because of rotational averaging, only one Fab of a stem antibody could be placed based on the cryo-ET data; the authors suggested that steric constraints may lower binding stoichiometry.** Amitai et al. (24) used molecular simulations to map the accessibility of HA epitopes to antibody binding on model virus-like particles (VLPs), and predicted that the rate of bivalent (avid) antibody binding to stem epitopes is much lower than that for head epitopes. The importance of bivalent binding in antibody maturation was demonstrated elegantly by Kanekiyo et al. (28), who co-displayed HA receptor binding domains (RBDs) from different influenza strains on nanoparticles (NPs). The heterotypic NPs (RBDs from multiple strains on an NP) elicited Abs with higher breadth than a mixture of homotypic NPs (RBD from a single strain on an NP). Because the vaccines differed only in the geometric arrangement of the antigens, and not in composition or proportion, the results imply that mosaic display confers an advantage to cross-reactive Abs *via* bivalent binding(28). Similar results were obtained recently for the SARS-CoV2 RBD.(29) **The importance of multivalent antigen binding in affinity maturation was also shown in the discovery of vaccine-induced Fab-dimerized antibodies directed to HIV glycans.(30)**

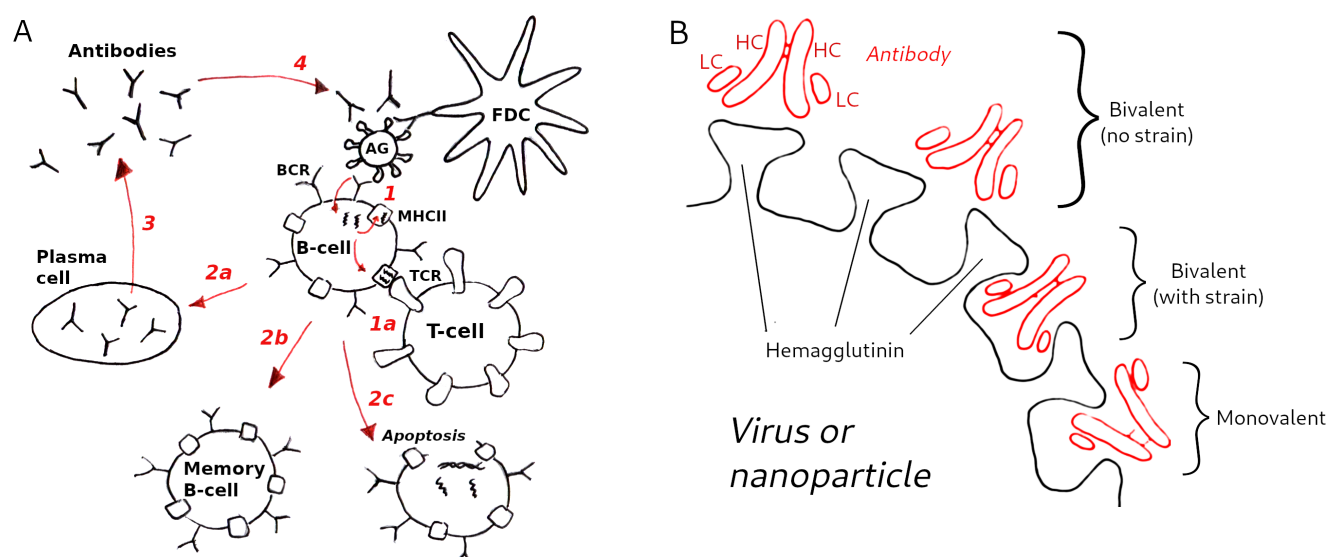


Figure 2. Schematic of the GC model used in this study. (A) Model overview: (1) B-cells are activated upon binding to antigen presented on follicular dendritic cells (FDCs, not explicitly modeled); (1a) in the optional T-cell help model (see text) B-cells are activated when the major histocompatibility complex receptor (MHC2) binds to the T-cell receptor (TCR); B-cell activation rescues B-cells from apoptosis, allowing them to mutate and proliferate; (2) depending on the activation signal, B-cells can differentiate to plasma cells (2a), to memory B-cells (2b), or undergo apoptosis (2c); (3) Plasma cells secrete antibodies (Abs), which also compete with B-cell receptors for antigen (4), which is the essential aspect of the Ab feedback model(31) (see text). (B) Hypothetical modes of antibody binding to influenza spikes; bivalent binding without strain (top) corresponds to cooperative binding by antibody arms; bivalent binding with strain (middle) corresponds to noncooperative binding; monovalent binding (bottom) is assumed to be the dominant mode of binding of anti-HA stem antibodies (see Methods for details).

Motivated by these studies, we employed a coarse-grained computer model of affinity maturation (AM) in GCs to investigate how avidity differences in the binding of B-cell receptors (BCRs) to their cognate antigens (AGs) could influence the patterns of immunodominance observed experimentally. Despite the coarse-graining, the model allows comparisons between multiple competing epitope/paratope pairs, in terms of B-cell and Ab production and affinity for antigen. We first show that the model is in qualitative agreement with experimental observations of the basic properties of GC reactions, and of the subdominance of influenza stem epitopes, whose predominant mode of binding to BCR/Ab is assumed to be monovalent. We then use the model to simulate multiple exposures to an antigen and interpret the results to propose strategies for overcoming immunodominance. We suggest that bnAbs that target subdominant epitopes are most likely to be elicited by increasing effective epitope concentration *via* design of custom immunogens or cocktail composition. The present model also predicts the resulting immune memory to be short-lived, which suggests that regular boosts may be required for vaccines composed of immunosubdominant epitopes.

Because the model and its computer implementation involve many technical aspects, we include the detailed Methods section at the end of the paper, after the Results and Discussion, which are presented next.

2 RESULTS

A visual schematic of the model is given in Fig. 2, and a brief overview is presented below. Complete details of the model equations and parametrization are given in Methods, and the parameter values used are listed in Table 1. Our approach is related to the differential equation models of Kepler and Perelson (32) and listed Oprea and Perelson (33). These models achieve a balance between biological detail and computational complexity: (i) they are sufficiently accurate to model the population sizes of B-cell receptors (BCRs) with different affinities, represented by discretized affinity classes; (ii) they contain a relatively small number of parameters, and (iii) they are simple enough to permit a large number of simulations to study the effects of different initial conditions or model parameters. (32, 33) More sophisticated approaches exist, which model individual interactions between immune complexes (ICs), Ags, BCRs and T-cells, aiming to capture GC reactions in higher detail. (34, 35) However, their use would be computationally prohibitive for this study. For example, modeling the case in which the initial BCR affinity to an antigen was drawn randomly from a distribution involved 8400 germinal center simulations, each 35 days in duration (see Results).

As in other models of affinity maturation, (36, 37) the interaction between BCRs and AGs is represented by a Langmuir isotherm that uses two equilibrium association constants, which represent binding of the first and second antibody arm. Unlike the more detailed models, (38, 24) the present model does not have an explicit structural component, and the effect of bivalency is reflected in the assignment of the association constants. Further, we simplify the biology by not distinguishing between centroblasts and centrocytes, nor between light and dark zones (LZ vs. DZ). Instead we consider the overall proliferation and death rates. This choice is motivated by the findings that the differences between centroblasts and centrocytes, and, more generally between the LZ and DZ, are smaller than previously thought; (39) *i.e.*, the physical boundary between LZ and DZ is rather diffuse, selection and proliferation can occur in both zones, albeit with different rates, and T-helper cells appear to be present in both zones, albeit in different proportions. Because we are interested in the dependence of the immune response on the number of competing BCRs with different binding valency and affinity, the model is parametrized to predict the following quantities: (i) the number of GC B-cells, (ii) the number of memory B-cells (MBCs), some of which can be recruited into secondary GCs, (iii) the number of plasma cells (PCs) that secrete Abs, (iv) the number of Abs, which compete with BCRs for antigen and implicitly regulate GC size, (31) and, optionally, (v) the T-helper cell population (which is discussed in Supplementary Material). The species (i)–(iv) are distributed into affinity classes, while the T-cell model uses two equilibrium affinities, those between TCRs and MHCII loaded or unloaded with peptides. The T-cell model is related to the T-cell expansion model of Mayer et al. (40). We consider the model to be optional for the simulations performed here, because **qualitatively the same results were obtained by assuming that the amount of T-cell help is equal to BCR activation by binding to antigen. However, the reason for the similar results could be the simplicity of our model, as we did not consider multiple distinct T helper cell populations, which were shown to be important for bnAb elicitation in a recent computational study. (41) Thus, in the main text, we present simulation results obtained without an explicit T-cell model. However, several validation calculations performed with the model are described in Supplementary Material.**

We first show that the model captures some experimentally determined properties of GCs. In Fig. 3 we compare the model results obtained with a single BCR/Ag pair to the average GC size reported by Wittenbrink et al. (42), and the MBC and PC production rates determined by Weisel et al. (44). The experimental data were also used by Pélissier et al. (43) to parametrize their stochastic GC model, which was used to explore the mechanism of clonal bursts. We note that the Wittenbrink et al. (42) observed very high CG size variability, as reflected in the experimental error bars (Fig. 3); thus, the agreement between

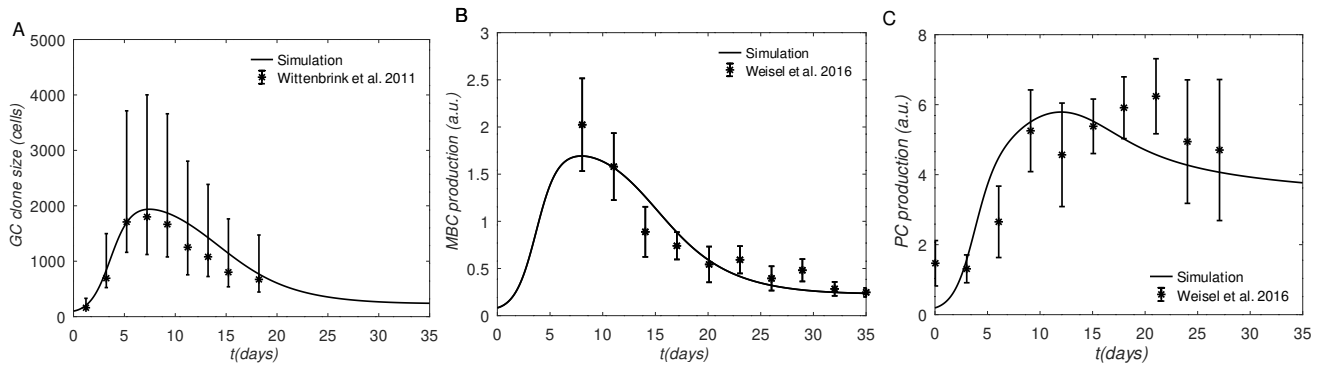


Figure 3. Comparison of simulation and experiments. A: Total B-cells, B: Memory B-cell production rate, C: Plasma cell production rate. Experimental data for panel A was generated from the GC cross-sectional areas plotted in Fig. S1B of Ref. 42, and converted to B cell counts as done in Ref. 43; The lower and upper error bars in panel A correspond to 30% and 70% quantiles, respectively; experimental data for panels B & C were taken from Fig. 4 of Ref. 43, who obtained raw data from Weisel et al. (44); the error bars in B & C correspond to approximately one SD, estimated from the range of the data, which we assumed to be Gaussian-distributed.

our model and the experimental average should be considered as a qualitative validation, as the model does not capture GC size heterogeneity.

One apparent disagreement is that rate of PC production in our model is accelerated by several days, compared to the data of Weisel et al. (44) (see Fig. 3C). Although the experimental MBC and PC production in Fig. 3B & C, respectively, correspond to the same time, matching the PC production rate in the simulation required shifting the experimental measurements by several days (compare Fig. 3B with Fig. 3C). However, the discrepancy is not expected to affect our results significantly, because we are interested in comparing the relative MBC output from different lineages at the end of GC reactions, which are simulated consistently, *i.e.* using the same model.

Next, we investigate the effects of BCR binding avidity under different scenarios. First, we compare the growth rates of three noncompeting B-cell lineages, which differ only in the value of the second-arm equilibrium binding constant K_{eq}^2 (written as K^{i2} for lineage i in Eq. (4) of Methods). This idealized scenario corresponds to three GCs evolving independently, which is the noninteracting, $\sigma=0$, case (see Methods, Sec. 4.0.5), each completely dominated by a single B-cell lineage.

We compare the behavior of lineages with three regimes of bivalency, corresponding to $K_{eq}^2=0$, $K_{eq}^2=K_{eq}^1$, and $K_{eq}^2=10K_{eq}^1$, which we denote, respectively, as the monovalent, noncooperative, and cooperative binding cases. The justification for the chosen values is discussed in the Methods Sec. 4.0.2.

The results in Fig. 4A show that the monovalent BCR has a significantly slower rate of growth compared with the bivalent BCRs, due to the reduced activation by Ag assumed by the model. In the monovalent case, the maximum B-cell count is less than a third of that in the bivalent cooperative case, and less than half of that in the noncooperative case; this lower maximum is also reached later; *i.e.*, after 20 days, *vs.* 5 to 7 days. Further, the MBC count at the end of the GC is reduced by half in the monovalent case, compared with the cooperative case (Fig. 4B), and the final average affinity of the B-cell population is several-fold lower (Fig. 4C). The delayed peak in the monovalent response is qualitatively consistent with the observations of Tan et al. (19), who noted that the anti-influenza stem Ab response was delayed by a week relative to the overall Ab response, and that the B-cell response was several-fold lower in magnitude.

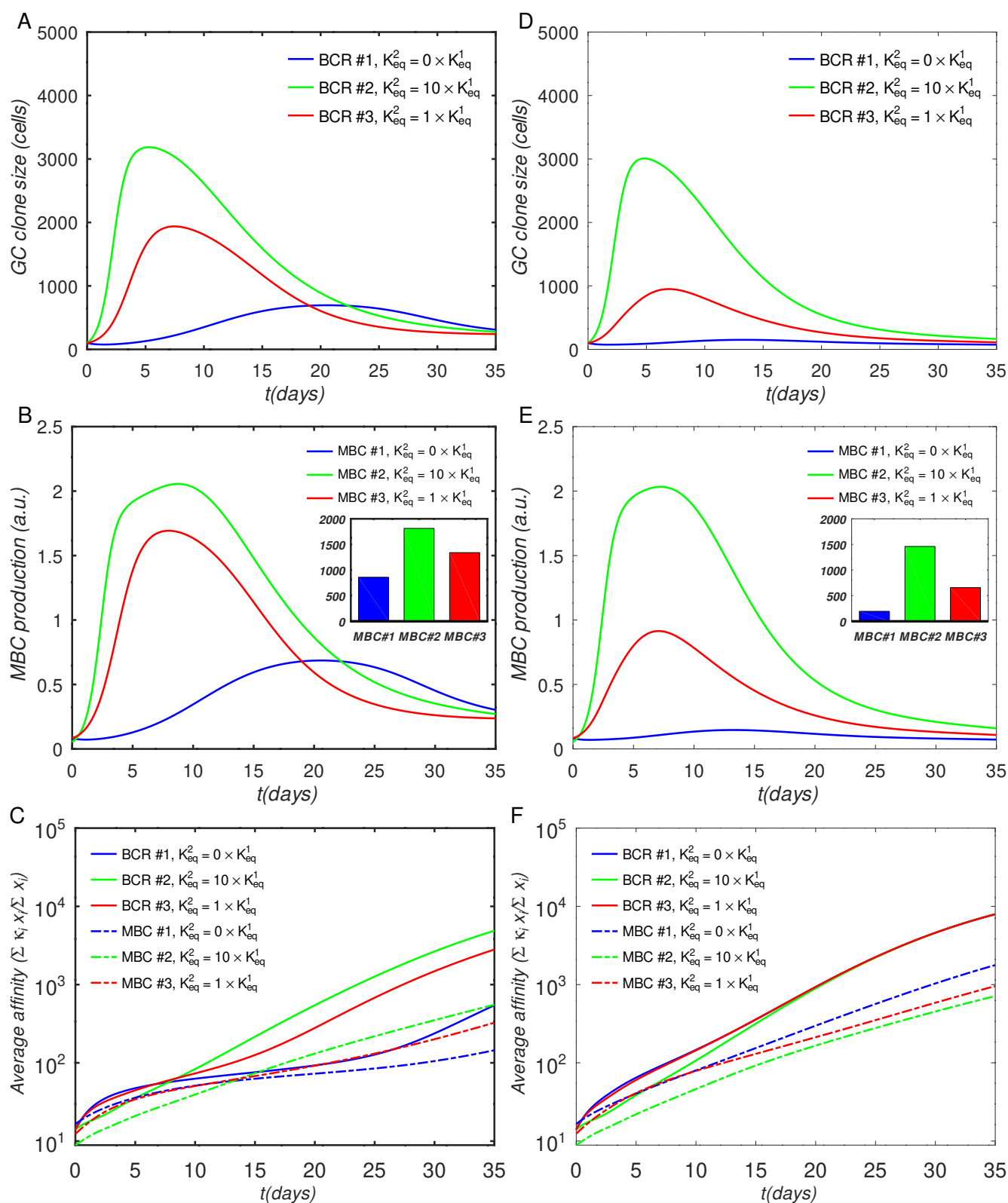


Figure 4. Effect of antibody valency and epitope occlusion on GC properties. Left column (A–C): noninteracting B-cell case ($o = 0$); Right column (D–F): fully interacting B-cell case ($o = 1$); A,D: Total B cells; B,E: Memory cell production rate; insets: total MBC population at end of simulation; C,F: Average affinity of B-cells and MBCs. For the definition of occlusion o , see Sec. 4.0.5.

Although the noninteracting GC case is illustrative, it is idealized, because in affinity maturation there will generally be many different B-cell lineages competing for epitopes on the Ags, or for T-cell help signals. Thus, a more realistic model of a single GC needs to account for competition between different lineages. As described in Sec. 4.0.5 we model this competition using an *occlusion* parameter o , with $o = 0$ for the fully noninteracting case, presented above, and $o = 1$ for the fully interacting (competing) case. **We note that a similar approach to model clonal competition was used by Yan and Wang (45), who introduced interaction parameters to represent Ag binding interference from Abs produced by earlier generations of B-cells.**

We describe the results of the fully interacting case ($o=1$) next; however, we note that a more realistic description of the overall GC reaction would probably involve intermediate values of o . For example, if, in some cases, different B-cells are able to bind to different epitopes on the same Ag simultaneously, the occlusion parameter would need to be less than 1, which would correspond to decreased competition between the B-cells. Moreover, when modeling multiple GCs, it may be necessary to include the possibility that the Abs secreted by the plasma cells can diffuse across many GCs, and compete with the 'local' BCRs for Ag.(31) This scenario would correspond to indirect competition between different B cell lineages in different GCs, which might be modeled with some optimized intermediate (though generally unknown) occlusion value. A possible starting point for estimating such a value could involve competitive binding experiments using antibodies specific for the different epitopes.

The simulation of the fully interacting case shows that the population disadvantage of the monovalent lineage is further increased (Fig. 4)D–F. The peak B-cell concentration of the monovalent lineage is more than 10-fold lower than that of the bivalent cooperative lineage (panel D). These results are to be expected, because the more rapidly proliferating lineage occludes the Ag, effectively reducing the amount of epitope available to the monovalent lineage. The average monovalent MBC production is lower by about a factor of eight relative to the bivalent cooperative case (panel E).

It is noteworthy that the average affinities of the three BCRs are indistinguishable after about 20 days after initiation of the GC reaction in the fully competing case (panel F). Further, the BCR affinities in this case at the end of the simulation are higher than those in the $o=0$ case (Fig. 4C vs. Fig. 4F). This result is understandable in terms of increased competition for survival inside the interacting ($o=1$) GC. The fact that binding by one BCR occludes access to other epitopes implies that the effective epitope availability is decreased for all BCRs. A decrease in the available binding sites increases the selection pressure on the BCRs, leading to the survival of the higher-affinity lineages. We will return to this point when we investigate the effects of varying epitope concentration explicitly. For completeness, simulation results with intermediate values of occlusion are shown in Fig. S1.

As discussed in the introduction, the reason for targeting immunosubdominant epitopes such as the influenza HA stem or the interfacial epitope(9) in vaccinations is their association with the elicitation of bnAbs, which are likely to provide protective immunity against future strains. In the context of the present simulations, such pre-existing protective immunity can be modeled by increasing the initial affinity of the monovalent antibodies, while keeping the other affinities unchanged. This gives the monovalent antibodies a survival advantage. A physiological rationale of setting a higher initial affinity of monovalent Abs could be that a significant proportion of monovalent (*e.g.*, anti-HA stem) MBCs are recruited into secondary GCs, where the higher initial affinity allows the MBC-derived blasts to compete more effectively with naïve bivalent B-cells. **A recent study that compared the early plasmablast (PB) response with GC B cells obtained by fine-needle aspiration from vaccinated human subjects found a variable, and sometimes large, clonal overlap (12% - 88%) between B cells in the PB pool and those in the GC,**

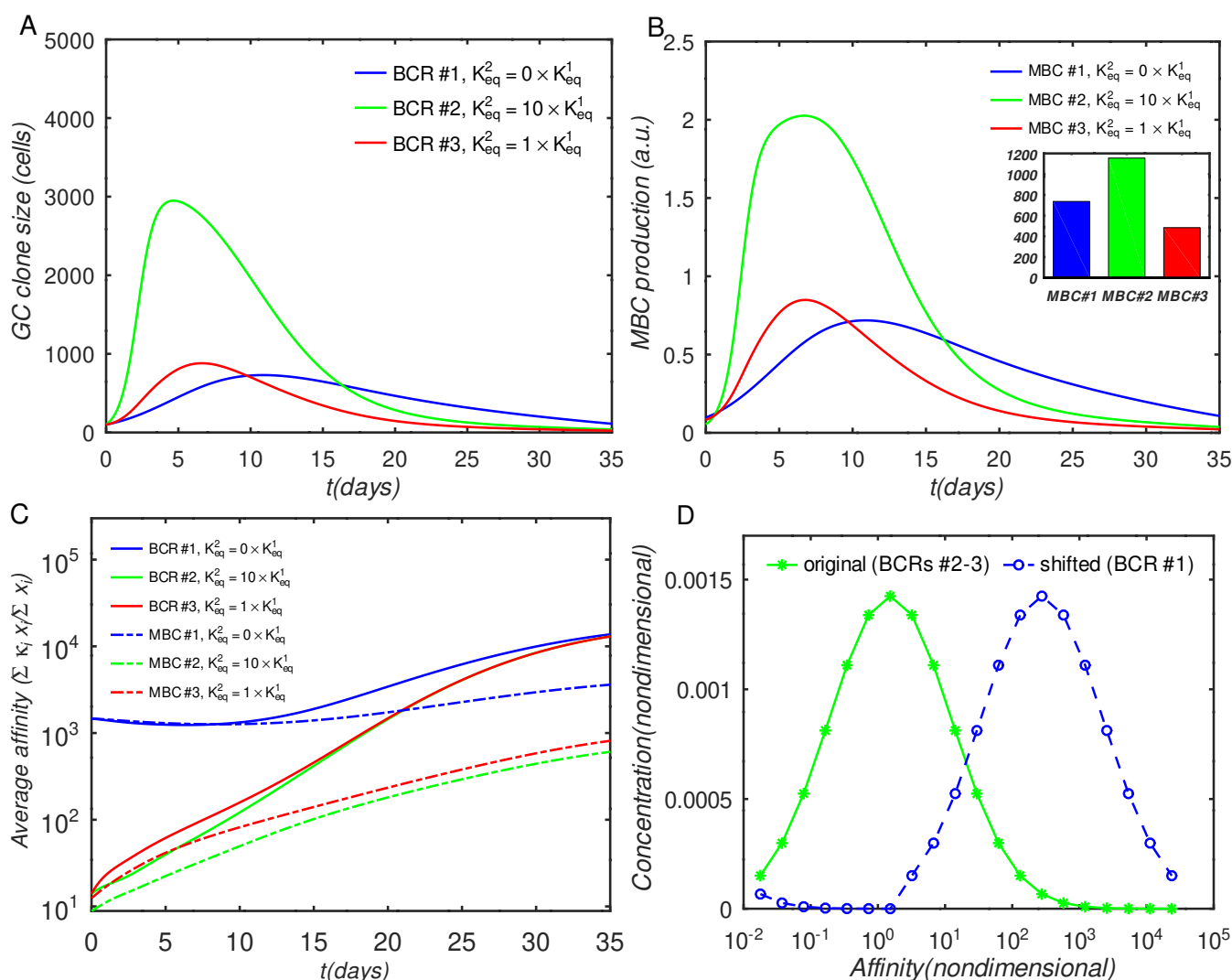


Figure 5. Effect of initial affinity advantage on the growth of monovalent B-cells in the fully interacting B-cell case ($\sigma = 1$). Panels A–C show the same quantities as Fig. 4A–C; The affinity distribution corresponding to BCR#1 was shifted toward higher values relative to BCR#2 and BCR#3 (panel D).

219 suggesting that substantial recruitment of MBCs into GCs is possible.(46) To model this scenario,
 220 we shifted the initial affinity distribution of the monovalent Abs by about two orders of magnitude towards
 221 higher values (see the distributions in Fig. 5D), and repeated the simulations for the fully interacting $\sigma=1$
 222 case (the $\sigma=0$ case is shown in Fig. S2).

223 Figure 5A shows that the population of the monovalent B-cells increased several-fold as compared
 224 with Fig. 4D (no advantage), such that, at their peak, these B-cells were almost as numerous as the
 225 bivalent noncooperative ones. However, even the large affinity advantage was insufficient to overcome
 226 the dominance of the cooperatively-binding Abs in terms of the total MBC response, which was still
 227 significantly lower in the monovalent case (Fig. 5B). Nachbagauer et al. (47) found that anti-HA stem
 228 immunity can be elicited or boosted upon immunization with chimeric HA constructs with HA heads
 229 to which the host is naïve, fused to HA stems against which there is preexisting immunity. In other
 230 studies,(48, 18) it was reported that boosting with HAs from pandemic, rather than with seasonally-drifted
 231 strains, boosted anti-stem immunity more effectively. The authors' interpretation of the results was that the
 232 vaccinations boosted preferentially anti-stem responses derived from MBCs, which were able to outcompete

the naïve response to the HA head. Further, Ellebedy et al. (18) also found that immunosubdominance of the stem reemerged after repeat immunization with the same pandemic strain.

To test whether the above findings could be explained with the present model, we systematically repeated the preceding simulations for different numbers of distinct BCR/epitope pairs (2 to 15), different occlusion values $o=[0,0.5,0.9,1]$, and three different values of affinity advantage provided to BCR#1 (given below); BCR#1 bound monovalently ($K_{eq}^{12}=0$) or bivalently ($K_{eq}^{12}=10K_{eq}^{11}$). The remaining BCR# i ($2 \leq i \leq 15$) were modeled as bivalent with $K_{eq}^{i2}=10K_{eq}^{i1}$. These simulations are discussed below, and their results are shown in Fig. 6.

The goal of the simulations is to approximate conditions in which one monovalent or bivalent anti-stem BCR (#1) lineage is evolving concurrently with 1-14 bivalent anti-head BCRs. In the first vaccination, all BCRs start from the same affinity distribution peaked at $K_{eq}^1 \simeq 1.53$ (Fig. 5D). To model the effect of stem conservation after the first vaccination, BCR#1 is given a (multiplicative) affinity advantage over the remaining BCRs of $\Delta K_{eq}=10, 100$, or 1000 . After the first (prime) simulation, each boost is initialized with a combination of 25% MBCs taken at the end of the previous simulation, and 75% naïve B-cells having the same initial distribution as that used for the prime. We assume that the previously-generated anti-head MBCs are poorly matched to the boosting Ag and shift their affinity distribution toward lower values by a factor of 1000, essentially eliminating any advantage of previous maturation. For the presumptive stem-directed BCR#1, we assume that the previously-generated MBCs are better matched to the boosting Ag, and shift their affinity downward only by a factor of 100, 10, or 1 (unchanged), to explore the effect of the mismatch; (thus, the affinity advantage ΔK_{eq} of BCR#1 corresponds to 1000 divided by 100, 10, or 1). We found that the proportion MBC#1 reaches a plateau by about five immunizations (see Fig. S3). In Fig. 6 we show the fraction of MBCs#1 after the sixth simulation.

First, we discuss the results of the cooperative bivalent anti-stem case (Fig. 6A). Here, BCR#1 does not have an avidity disadvantage (since it is cooperatively bivalent with $K_{eq}^{12}=10K_{eq}^{11}$), relative to the remaining BCRs, and has an affinity advantage, as described above. In the noncompeting case ($o=0$) the MBC fraction $\zeta = MBC_1 / \sum_{i=1}^{N_B} MBC_i$ is not very sensitive to the affinity advantage, because the Abs are maturing independently and the concentration of each epitope is the same. As the competition between the BCR lineages is increased, the affinity advantage becomes more important. For example, in the high occlusion cases $o \geq 0.9$, with 9 competing low-affinity BCRs, a 1 to 3 order of magnitude affinity advantage results in $\sim 20\%$ to $\sim 50\%$ of the final MBC population being derived from BCR#1 ($\zeta \in [0.2, 0.5]$ in the two right panels of Fig. 6A).

In contrast, the monovalent anti-stem response (Fig. 6B) produces markedly lower, though still significant MBC#1 proportions. For the lowest initial affinity advantage ($\times 10$), the proportion of MBC#1 is vanishingly small for all interacting cases. For the higher advantage values ($\times 100$ and $\times 1000$), the proportion of MBC#1 with 9 competing low-affinity BCRs at $o \geq 0.9$ is in the range $\sim 10\% - \sim 30\%$ ($\zeta \in [0.1, 0.3]$ in the two right panels of Fig. 6B).

We interpret these results to suggest that a previous response to a conserved epitope could be boosted to dominate the subsequent response, even in the presence of a significant number of poorly-conserved ‘distracting’ epitopes. This is consistent with the chimeric vaccination results of Nachbagauer et al. (47). However, the extent of boosting is critically dependent on the affinity advantage of the preexisting immunity. In the case of monovalent antibodies, the affinity advantage needs to be high to overcome the proliferation disadvantage caused by monovalency, and the entropic disadvantage caused by distracting epitopes that generally outnumber conserved ones. Ellebedy et al. (18) noted that vaccination with a pandemic strain

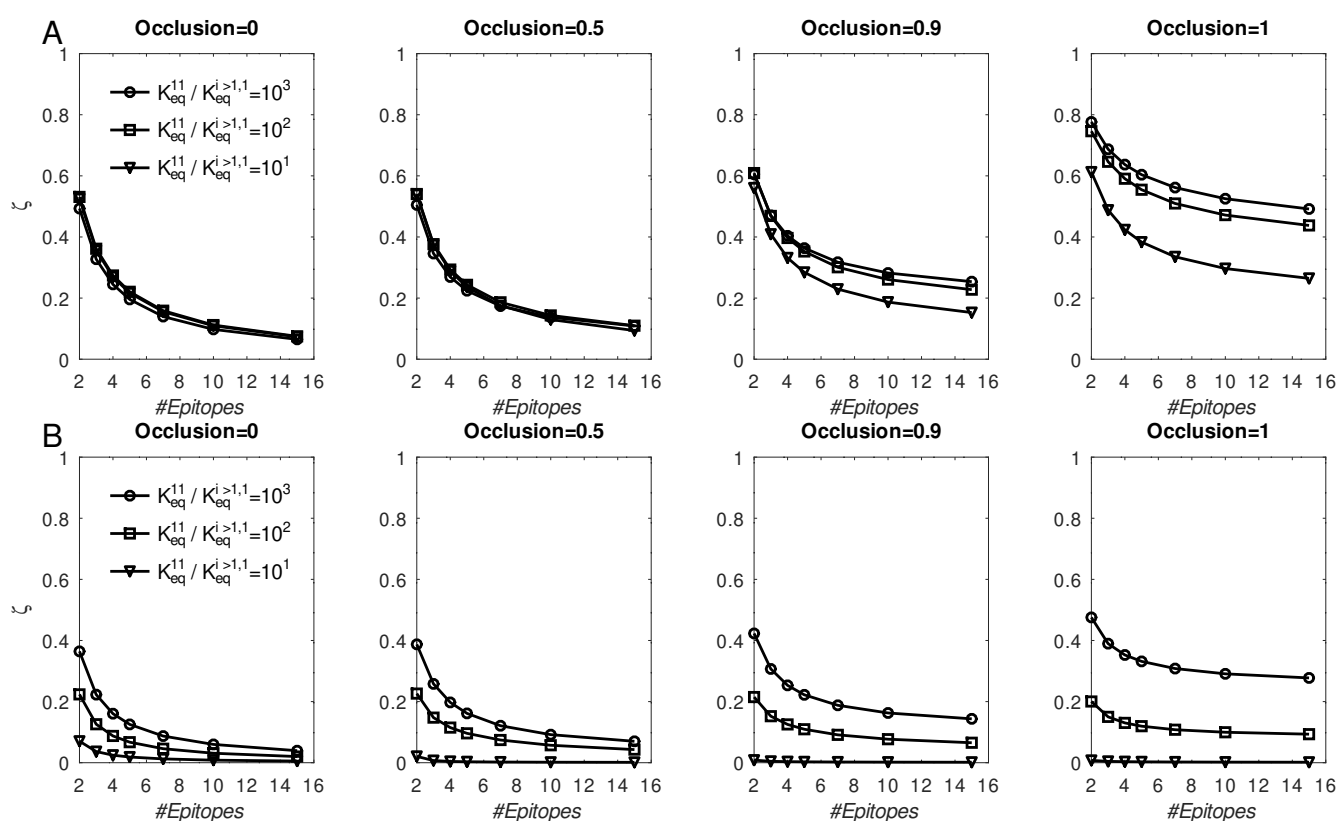


Figure 6. Fraction of MBC#1 (ζ , defined in the text) at the end of six GC simulations for different initial affinity advantage values vs. total number of BCR/Epitope pairs. A: BCR#1 is cooperatively bivalent ($K_{eq}^{12}=10K_{eq}^{11}$); B: BCR#1 is monovalent ($K_{eq}^{12}=0$).

276 against which anti-HA head immunity is low, preferentially boosted anti-HA stem antibodies. However,
 277 upon reimmunization with the same antigen, the anti-HA head Abs were boosted preferentially. These
 278 results can be rationalized in the present model by the differential affinity advantages of the anti-HA stem
 279 Abs. Specifically, for the first immunization, the anti-stem immunity has a sufficient affinity advantage
 280 to overcome the growth-related and entropic disadvantages. For the second immunization, the affinity
 281 advantage is eroded because the anti-HA head immunity has undergone affinity maturation caused by the
 282 first immunization, which leads to the restoration of stem epitope subdominance.

283 Because the affinity advantage of a conserved epitope cannot be predicted accurately if antigenic drift is
 284 present, a more realistic approach would be to treat ΔK_{eq} as a random variable. To investigate this scenario,
 285 we performed a round of simulations in which ΔK_{eq} was sampled from the lognormal distribution; the
 286 results are described in Supplementary Material S1. The differences between the two cases were similar
 287 to those in the simulations with fixed ΔK_{eq} . For example, in the bivalent case, some MBC#1 cells were
 288 always present, while in some simulations of the monovalent case the MBC#1 proportion is near zero (see
 289 Fig. S4).

290 The above simulations suggest that an affinity advantage alone will not always be sufficient to overcome
 291 the disadvantage of slower proliferation and entropic distraction. This result, together with other factors,
 292 such as low germline precursor frequency or T-cell help insufficiency,(19) could explain the lower
 293 prevalence of anti-HA stem immunity.

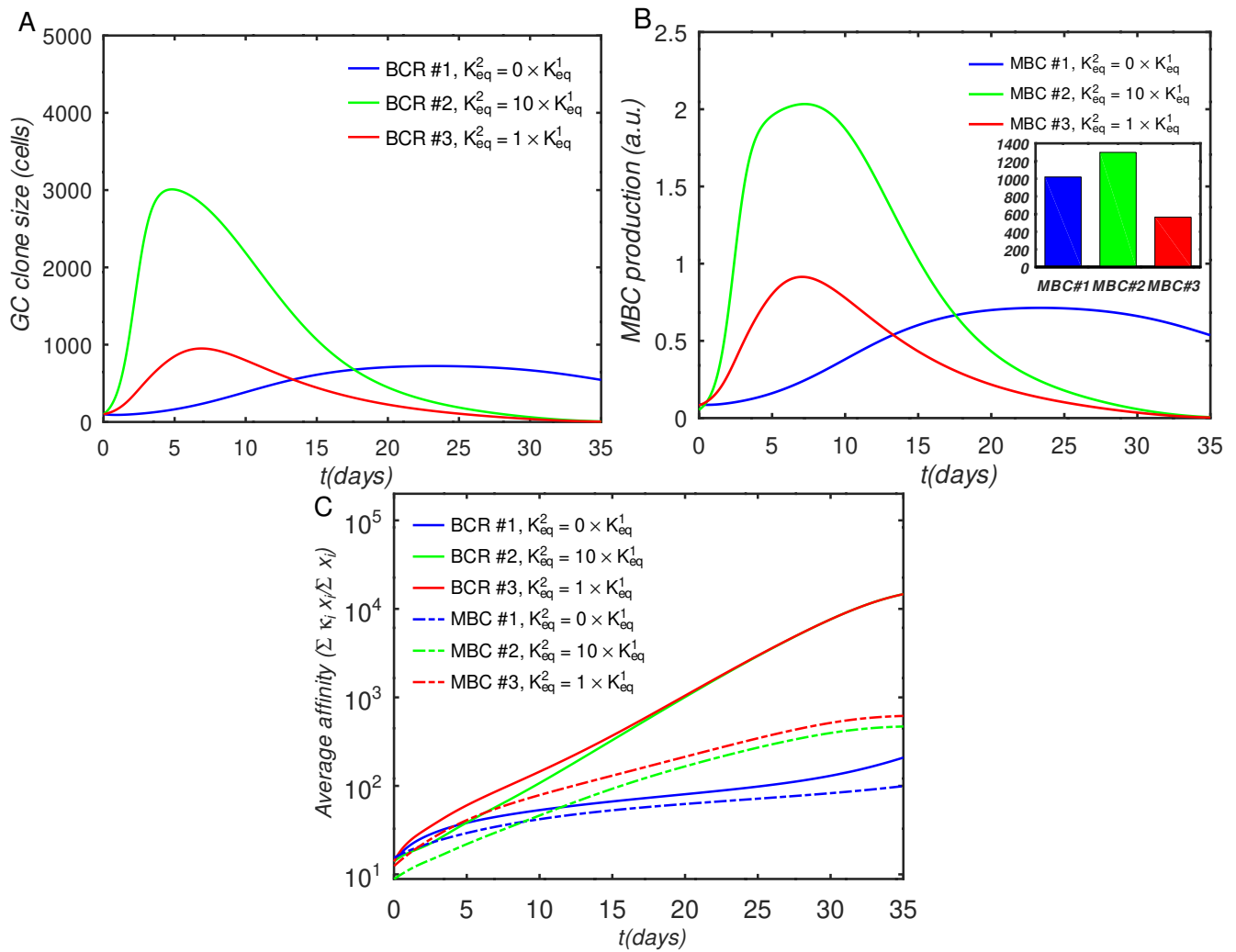


Figure 7. Effect of BCR valency and epitope concentration on GC evolution, with $\sigma = 1$ (fully competitive case). Panels A–C show the same quantities as Fig. 4A–C; $\alpha_1^T = 2$, $\alpha_2^T = 1$, $\alpha_3^T = 1$; α^T is the nondimensional total Ag concentration (see Sec. 4.0.6).

294 In natural infections, the epitope concentrations are predetermined by the Ag itself (*e.g.*, the solvent-
 295 accessible surface area of the HA head on an influenza virion is about twice that of the stem; see
 296 Fig. S5 in Supplementary Material S2). However, the vaccination setting allows use of designed antigens
 297 with some epitopes masked by glycosylation(10, 49, 50) or even completely removed using protein
 298 engineering(51, 52). Additionally, one can administer concurrently multiple Ags, in which some Ag
 299 epitopes are sufficiently conserved between the antigens that they can be considered to represent a single
 300 epitope with a higher effective concentration. (28, 53, 29, 26). In the next set of simulations, we investigate
 301 the interplay of epitope concentration and BCR binding valency. Figure 7 shows the results of a GC
 302 simulation involving three competing BCR/Ag pairs, for comparison with the previous 3-BCR simulations
 303 (Figs. 4 and 5); the noninteracting case can be found in Fig. S6. The concentration of Ag#1, which
 304 corresponds to the monovalent BCR#1, was twice that of the other two Ags, while all other parameters
 305 were the same as in the original 3-BCR simulation. The peak monovalent B-cell population increases
 306 several-fold relative to the uniform concentration case (Fig. 4D); it is similar in magnitude to that in the
 307 affinity-advantaged case of Fig. 5, but occurs later, at ~ 23 vs. ~ 11 days. This behavior was expected,
 308 because, although BCR#1 has an impaired growth rate due to monovalency, it also has more antigen

309 available, allowing it to grow for longer times. Even though the other (bivalent) BCRs are occluding, the
310 higher concentration of Ag#1 overcomes the occlusion disadvantage, albeit with a slow growth rate. The
311 resulting MBC#1 population is much closer to that of the bivalent cooperative case. However, although the
312 greater abundance of Ag#1 amplifies the total BCR#1 response, it also reduces the competition for this Ag,
313 which results in a lower overall affinity of the resulting B-cells (Fig. 7C).

314 For completeness, in Supplementary Material S3 we repeated the above simulation while systematically
315 varying the number of BCR/epitope pairs (2-15), occlusion parameter value (0,0.5,0.9,1), with three values
316 of affinity advantage provided to the BCR#1, and with the BCR#1s bound monovalently or bivalently.
317 The results are summarized in Fig. S7. In all cases, increasing Ag concentration leads to greater MBC
318 output, with the increase being larger if the corresponding BCR also has a significant affinity advantage.
319 The increased MBC output is associated with decreased affinity, however, and the affinity decrease is
320 larger for monovalent than bivalent BCR#1s. The results therefore suggest that epitope subdominance
321 can be overcome by increasing epitope concentration in vaccinations with cocktails of designed antigens,
322 as proposed by others.(28, 29, 26) However, this is achieved at the expense of a reduction in the affinity
323 of the resulting MBCs. For vaccine design, the precise Ag concentrations may need to be optimized to
324 achieve a compromise between MBC population size and affinity for antigen. **We caution, however, that**
325 **the above results should be considered qualitative because our model does not incorporate a**
326 **saturating Ag concentration, which could be done in future versions, e.g., by explicitly modeling**
327 **immune complexes or FDCs. Thus, the strong dependence of the B-cell response on the Ag**
328 **concentration is most likely relevant in a scenario where the total antigen amount is low.**

329 Finally, to investigate whether the outcome of multiple vaccinations can be optimized by manipulating the
330 epitope concentrations corresponding to monovalent BCRs, we simulated six consecutive immunizations
331 under the same initial conditions as described before, except that the concentration of Ag#1 was increased
332 in some, but not all, of the simulations. Specifically, we considered three immunization scenarios, in which
333 the total nondimensional concentration of Ag#1, $\alpha_1^T = [\text{Ag\#1}/\text{Ag\#i} > 1]$, in the six consecutive immunizations
334 was (1, 1, 1, 1, 1, 1), (2, 1, 1, 2, 1, 1), and (2, 2, 1.5, 1.1, 1, 1). These three scenarios were chosen to
335 determine whether increased Ag#1 occurring early in a vaccination regimen would translate into superior
336 responses in later exposures. Figures 8 and S8 show the MBC output and affinity, respectively, at the end
337 of each immunization for ten BCR/epitope pairs (other cases are omitted for clarity, but are qualitatively
338 similar). Consistent with the previous results, MBC#1 output after a particular immunization increases
339 if Ag#1 used in that immunization is increased (and vice versa), and the MBC#1 affinity decreases if
340 Ag#1 used in that immunization is increased (and vice versa). However, the differences between the three
341 protocols essentially disappear after the final exposure, hence the present model suggests that there may not
342 be a significant long term immunological effect of simply manipulating antigen concentration in a vaccine.

343 **We also note that, in the idealized case of a uniform antigen concentration profile, the normalized**
344 **BCR affinities for antigen rise uniformly to a plateau around the 5th exposure (Fig. S8). However,**
345 **the results show a sensitivity to the antigen concentration profile, suggesting that the number of**
346 **exposures needed to elicit high-affinity antibodies depends on the details of the exposure, such**
347 **as epitope concentration, or whether the exposure is by vaccination or natural infection.**

3 DISCUSSION

348 Rapidly mutating and proliferating viruses such as influenza, HIV, and, more recently, SARS-CoV-2,
349 accumulate escape mutations that can render existing host immunity obsolete. However, because such

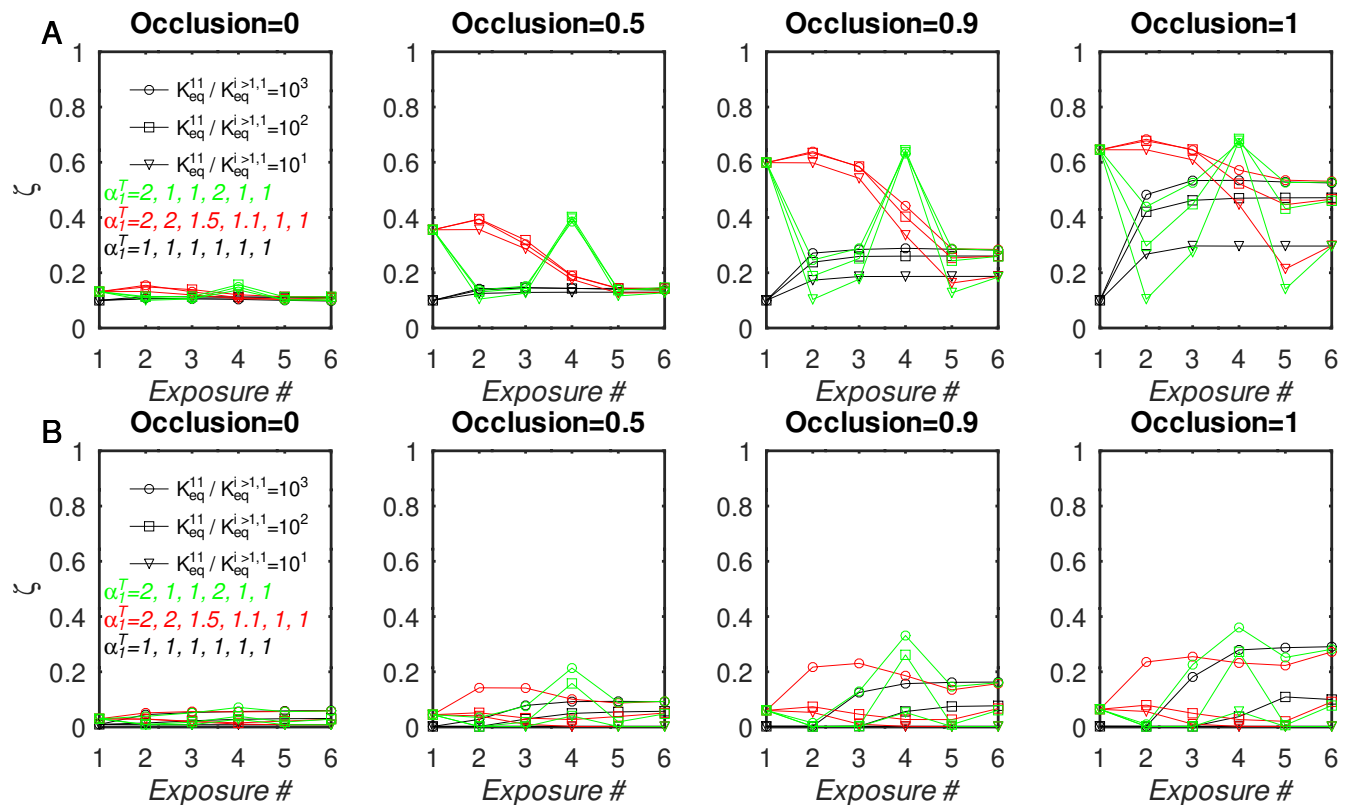


Figure 8. Fraction of MBC#1 vs. number of sequential GC simulations for different initial affinity advantage values and different Ag#1 concentrations, with 10 total BCR/Epitope pairs. A & B: MBC#1 fraction (ζ) at the end of simulations. A: BCR#1 is cooperatively bivalent ($K_{eq}^{12}=10K_{eq}^{11}$); B: BCR#1 is monovalent ($K_{eq}^{12}=0$). The four sets of panels A and B show the effect of increasing occlusion from $o=0$ (no competition) to $o=1$ (full competition).

350 pathogens must maintain infectivity to survive, some mutations are highly improbable, as they would
 351 significantly reduce or even eliminate viral fitness. In addition, selection pressure from the immune system
 352 is variable along the antigenic sequence (*e.g.* solvent-exposed regions are more susceptible to antibodies
 353 than buried ones). The resulting differences in mutation propensities make it possible to partition the viral
 354 topology into variable and conserved epitopes. Unfortunately, variable epitopes tend to be immunodominant,
 355 *i.e.* they are the main targets of adaptive immunity. Immunodominance, in itself, may be the result of
 356 viral adaptation; for example, the large highly-variable head of influenza hemagglutinins is an entropic
 357 distraction to the immune system. A major focus of current vaccine research is to elicit a potent and durable
 358 immunity to conserved, immunosubdominant, epitopes. Such vaccines would lower HIV infection rates, or
 359 eliminate the need for a yearly influenza vaccine.

360 Here, we employed a coarse-grained model of affinity maturation (AM) parametrized using experimental
 361 data on germinal centers (GCs)(42, 44, 43) to determine whether differences in B-cell receptor (BCR)
 362 binding valency could explain the subdominance of certain epitopes. The main assumption of the model
 363 is that B-cell activation increases with the amount of equilibrium-bound BCR to antigen (Ag). More
 364 specifically, when both arms (Fabs) of BCR bind the antigen displayed on follicular dendritic cells
 365 (FDCs), the probability of internalizing the Ag increases, even if the affinity of each receptor for Ag is
 366 weak. This assumption appears to be in accord with the experiments; Arevalo et al. (20) interpreted their
 367 vaccination boosting data by suggesting that many weak BCR/Ag interactions are sufficient to activate

368 B-cells. Compelling indirect evidence comes from co-display of different Ags on nanoparticles, which
369 was demonstrated to preferentially elicit broadly-neutralizing Abs. These findings(28, 29) imply that avid
370 bivalent binding confers a proliferation advantage, which is consistent with the present model. However, as
371 B-cell activation by Ags is a complicated process, involving cross-linking of the BCRs, it is not clear to
372 what extent avid binding would increase crosslinking. Future experiments and simulations may be needed
373 to shed more light on the activation process.

374 The present simulations indicate that monovalent B-cells always grow more slowly than bivalent ones,
375 and are therefore easily dominated by B cells that are able to bind bivalently and cooperatively. When
376 given an initial affinity advantage over bivalent B-cells, as might be expected to occur upon recruitment
377 of monovalent memory cells (MBCs) into secondary GCs, the affinity advantage was often insufficient
378 to overcome the slower growth. The monovalent B cells outcompeted bivalent ones only if the affinity
379 advantage was more than an order of magnitude (see Fig. 6B). These results are in agreement with influenza
380 vaccination experiments, which show that a boost with a pandemic strain for which the host has little
381 immunity against epitopes in the HA head, produces high anti-HA stem titers; a subsequent boost with
382 the same vaccine elicits anti-HA head Abs.(18) We have interpreted these experimental data by assuming
383 that anti-HA stem Abs bind monovalently with a high affinity advantage in the first vaccination, but not
384 the second. In the second vaccination, the bivalent anti-HA head Abs are able to overcome the advantage
385 *via* maturation induced by the first shot.

386 Rather than relying solely on an affinity advantage, a more robust method to boost monovalent B-cells
387 is to increase the concentration of their cognate epitope(s). The simulations indicate that this approach
388 results in the highest number of monovalent MBCs (see Figs. 7 and 8 in Sec. 2). The finding is not
389 surprising, since the presence of foreign antigen is what initiates and sustains GC reactions in the first place.
390 However, because selection among B-cells is driven by competition for Ag, an increase in available Ag
391 will allow lower-affinity BCRs to survive. Thus, although the corresponding monovalent Abs become more
392 numerous with increased epitope concentration, they evolve lower average affinity. When we simulated a
393 subsequent GC reaction initialized with MBCs from such a memory pool, but *without* the concentration
394 advantage (designated by $\alpha_1^T = 1$ in the results), as would occur in a natural infection, the monovalent
395 B-cell population rapidly decreased, such that after two such consecutive GC reactions, there was no
396 difference when compared to vaccinations in which the concentration of the Ag cognate to the monovalent
397 Ab was never increased (Fig. 8).

398 These results suggest that increasing Ag concentration might only provide a temporary advantage to the
399 cognate BCRs, as Ag levels are easy to manipulate in vaccination, but not in infection. **Nevertheless, the**
400 **strategy could prove useful to expand the number of initial low-affinity B-cell lineages targeting**
401 **rare epitopes against which high-quality B-cell precursors are rare, such as group I and II influenza**
402 **stem epitopes, as also suggested in a recent computational study of COVID vaccine efficacy.(54)**
403 If subsequent exposures *via* natural infection restore immunosubdominance,(18) regular vaccine boosting
404 with higher concentrations of subdominant epitopes could be required.

405 **We note that multi-antigen vaccination cocktails have been designed, in which the epitopes**
406 **that are conserved between the antigens are at effectively higher concentration than variable**
407 **epitopes.(28, 29, 26) In particular, mosaic nanoparticles appear to elicit a broader antibody**
408 **response in animal experiments, compared to cocktail immunizations.(28, 29) However, it remains**
409 **to be shown whether such vaccines will lead to improved protection against highly mutable**
410 **pathogens in the clinic.** Simulations performed here suggest that such cocktails have promise to elicit

411 Abs to conserved epitopes *via* a concentration advantage. Future experiments are needed to address whether
412 the resulting immunity would persist after multiple rounds of natural infections.

413 The model used here relies on simple assumptions to show that for different epitopes
414 with similar accessibilities, which can be interpreted as similar effective concentrations,
415 immunosubdominance can be explained by differences in the antibody binding valency. This
416 scenario appears applicable to the case of natural immunity against influenza hemagglutinins,
417 as Harris et al. (27) have shown that most of the trimeric HA spikes are able to bind an anti-
418 stem antibody. The arrangement of the spikes makes it likely that bivalent binding would be
419 disfavored by energetic strain.(27, 24) A related scenario applies in the case of HIV, in which
420 low spike density makes bivalent binding unlikely, but antibodies engineered with long linkers
421 that could bind the same trimeric spike bivalently exhibited > 100 -fold greater potency.(55)
422 However, binding valency alone cannot explain immunodominance that arises in vaccination
423 using soluble HA ectodomains because head and stem epitopes would be expected to have
424 similar antibody accessibilities. Therefore, other factors, such as antigen plasticity, low natural
425 germline precursor frequency, repertoire filtering due to self-reactivity, or reduced T-cell help,(41)
426 must also contribute. For example, Keating et al. (56) employed several methods of partially
427 inhibiting GC formation in mice, and showed that the proportion of bnAbs in GC-inhibited mice
428 was not increased relative to wild-type mice or untreated mice. These findings were used to argue
429 that the predominant reason for low bnAb prevalence was not competition between antibody
430 lineages within GCs, but rather other factors, such as removal of bnAb precursors due to immune
431 tolerance mechanisms.(56) Such factors could also explain why antibodies produced in natural
432 infections such as SARS-Cov-2 tend to target relatively few antigenic epitopes, despite high
433 overall antigen accessibility.(57)

434 Some of the aforementioned factors could be incorporated into the model in an approximate way in future
435 studies. The effects of adjuvants on B-cell activation can be modeled by parametrizing the B-cell
436 activation function h (see Methods) to include adjuvant concentration, or by incorporating the latter
437 into a T helper cell model. Similar ideas could be used to include the effects of soluble signaling
438 species, such as interleukins or Calcium ions. Further, more sophisticated approaches that
439 explicitly model BCR evolution in sequence space and/or compute BCR/Ag binding affinity using
440 structural models have been developed. For example, Robert et al. (58) approximated B-cell and
441 antigen interactions by discretizing the epitope and paratope on a lattice, and using an empirical
442 inter-residue potential.(58) The authors were able to capture key properties of multi-antigen
443 vaccinations, such as increased cross-reactivity in cocktail immunizations. However, BCR/Ag
444 models at all-atom resolution,(59, 60) which may be parametrized to account for antigen stability
445 and rigidity, may ultimately be required to design actual vaccine antigens and their cocktails.

446 For the practical purpose of universal vaccine design, we can summarize the interpretation of
447 our simulation results as follows. HA stem epitopes presented on influenza virions are immuno-
448 subdominant due to an inability to recruit bivalently-binding BCRs, combined with other causes
449 of subdominance. Even if vaccination with soluble antigen ectodomains elicited an anti-stem
450 response, it would not be boosted in secondary GCs formed upon subsequent natural reinfection,
451 because the corresponding B-cells would be unable to bind antigen bivalently. It remains to be
452 shown whether this disadvantage could be overcome by devising vaccines that present stem
453 epitopes for bivalent binding, *e.g.* by using engineered immunogens attached to nanoparticles,(52)

possibly in a mosaic arrangement(29), or by immunizing with cocktails with very similar stems but diverse heads(26).

While immunization with diverse coronavirus receptor binding domains presented as mosaic nanoparticles elicited a broad antibody response, including to strains not present in the vaccine,(29) when this strategy was applied to a diverse panel of influenza HA spikes, the resulting breadth was no greater than that observed with immunizations using homotypic nanoparticle cocktails.(61) The interpretation was that the epitopes in the mosaic panel were too dissimilar to allow significant bivalent binding, which suggests that careful tuning of antigen sequence similarity may be needed to elicit broad responses *via* a concentration advantage.

4 METHODS

4.0.1 Model of Germinal Center Affinity Maturation

The model of affinity maturation (AM) used here is based on the work of Kepler and Perelson (32), who used systems of coupled differential equations to calculate the concentrations of B-cells of different discrete affinities for an antigen (Ag). We have generalized the model to simulate the maturation of multiple B-cell lineages, each binding to its cognate antigen mono- or bivalently, and producing memory B-cells and plasma cells, which secrete antibodies of the same affinity for the cognate Ag. The model does not have any geometric or topological component to represent binding, and, where there is no ambiguity, we sometimes use the terms antigen and epitope interchangeably. We will also sometimes use the abbreviation BCR (B-cell receptor) to refer to B-cells, with the implicit scaling assumption that each B-cell has $\sim 10^5$ BCRs on its surface.(62, 63)

We assume that the simulated germinal center(s) (GCs) have been seeded by N_B B-cell lineages B^i , and that each lineage can bind only to its cognate antigen a_i . Though the model is based on the system of differential equations of Kepler and Perelson (32), it has several important additions, notably memory cell, plasma cell, and antibody production. For clarity, we first present a minimal version of the model, which is close to the original B-cell model(32) and describe the modifications in subsequent subsections.

4.0.1 Basic model

For each B-cell lineage, we explicitly model its binding affinity distribution. Specifically, we assume that (1) the equilibrium binding affinity K_{eq}^i of any B-cell B^i derived from the lineage i for its cognate antigen a_i is in the range $K_{eq}^{min} \leq K_{eq}^i \leq K_{eq}^{max}$ and (2) that the affinities can be represented by a discrete set of values, as follows. We assign to each B^i a binding energy index $j \geq 1$ such that

$$\log K_{eq}^{min} \leq (j-1)\Delta E + \log K_{eq}^{min} \leq \log K_{eq}^i < j\Delta E + \log K_{eq}^{min} \leq \log K_{eq}^{max} + \Delta E. \quad (1)$$

Equation (1) corresponds to a uniform discretization of binding affinities in logarithmic space with energy grid spacing ΔE , or exponential discretization in affinity space.

As done by Kepler and Perelson (32), we will refer to the energy bins j as *affinity classes*. Their number, N_ϵ , is related to ΔE by $\log K_{eq}^{max} - \log K_{eq}^{min} = (N_\epsilon - 1)\Delta E$. We take $N_\epsilon=20$ (see Table 1), which implicitly determines ΔE once K_{eq}^{min} and K_{eq}^{max} are chosen. In the simulations, we only allow values of K_{eq} that correspond to the bin edges, *i.e.*, $K_j^i = K_{eq}^{min} e^{(j-1)\Delta E}$, $1 \leq j \leq N_\epsilon$, where, for brevity, we replaced the subscript eq by the affinity class index j .

490 To simulate affinity maturation, we compute the time evolution of B-cell populations in each affinity
 491 class j using

$$\frac{d[B_j^i]}{dt} = \{-k_d(1 - h_j^i) - k_p\} [B_j^i] + 2k_p \sum_{k=1}^{N_\epsilon} m_{kj} [B_k^i], \quad (2)$$

for $1 \leq i \leq N_B$,

492 where k_p and k_d are proliferation and death constants, respectively, m_{kj} is the probability for a BCR B^i in
 493 affinity class k to transition to affinity class j via somatic mutations that take place during AM, h_j^i is B-cell
 494 activation function (discussed below), and N_B is the number of different B-cell lineages.

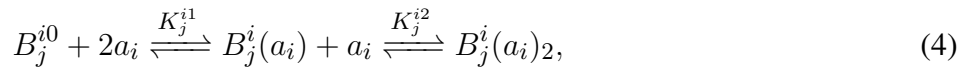
495 The class transition probabilities m_{jk} are assumed to be independent of the lineage i , and are defined as

$$m_{jk} = \frac{[\mu(1 - p_L)]^{|k-j|}}{|k-j|!} \frac{\exp(-\mu)}{1 + \Lambda^{2(k-j)}}, \quad j \neq k$$

$$m_{jj} = 1 - \sum_{k \neq j}^{N_\epsilon} m_{jk}, \quad (3)$$

496 where Λ determines the ratio of advantageous to non-lethal deleterious mutations, p_L is the probability
 497 of lethal mutations, and μ is the probability of an expressed (*i.e.* nonsilent) mutation per generation.(32)
 498 Kepler and Perelson (32) used an oscillating function for $\mu(t)$ to mimic the effect of interconversion of
 499 centroblasts and centrocytes on the mutation rate, which was optimized to maximize a ‘total’ affinity $A(t)$
 500 of mature B-cells of a single lineage $i=1$ ($A(t) = \sum_j^{N_\epsilon} [B_j^1] K_j^1$). We use a constant average mutation rate
 501 $\mu=0.1$, which is appropriate for comparing growth rates of different BCR lineages within the framework of
 502 this coarse-grained model; otherwise one would need to specify the phases of oscillation for each lineage,
 503 which are unknown, and might furthermore be stochastic. The constant value $\mu=0.1$ was also used by
 504 Oprea and Perelson (33).

505 The activation function h_j^i is derived from the proportion of the B cells, B_j^i , that receive a survival signal
 506 via binding to antigen and/or helper T-cells (Tfh). In the simpler model, which involves only activation by
 507 antigen (Ag), h_j^i is computed from the equilibrium fraction of receptors B_j^i bound to the cognate Ag a_i .
 508 Because each BCR has two binding arms (Fabs), we assume the binding reactions



509 corresponding to sequential binding of the first and second Ags to free B-cells (B_j^{i0}). From the conservation
 510 of total B cells B_j^i ,

$$[B_j^{i0}] + [B_j^i(a_i)] + [B_j^i(a_i)_2] = [B_j^i], \quad (5)$$

511 we have

$$[B_j^i(a_i)] = \frac{K_j^{i1} [B_j^i] [a_i]}{1 + K_j^{i1} [a_i] (1 + K_j^{i2} [a_i])} \quad (6)$$

512 and

$$[B_j^i(a_i)_2] = \frac{K_j^{i1} K_j^{i2} [a_i]^2}{1 + K_j^{i1} [a_i] (1 + K_j^{i2} [a_i])}, \quad (7)$$

which allows us to compute the fraction of bound BCR arms (two per BCR), provided that the concentration of free Ag, $[a_i]$, is known, *i.e.*

$$\theta_j^i = \frac{[B_j^i(a_i)] + 2[B_j^i(a_i)_2]}{2[B_j^i]}. \quad (8)$$

In the above, K_j^{i1} and K_j^{i2} are equilibrium binding constants, corresponding to binding by a first BCR arm and the second, respectively. K_j^{i1} is equal to the affinity of the Fab, *i.e.*, $K_j^{i1} = K_j^i$, and K_j^{i2} is taken to be proportional to it, $K_j^{i2} = C_i K_j^i$, where the constant C_i is affinity-independent, and reflects geometry-related factors that influence the binding of the second arm, such as excluded volume (entropy), and deformation strain (energy) required to position the second arm for binding. Monovalent binding corresponds to $C_i = 0$. Other values of C_i used in the simulations were 1 and 10, which are discussed in the next subsection.

To evaluate Eqs. (6) and (7), $[a_i]$ is needed. Writing conservation of total antigen $[a_i^T]$, which is prescribed at the beginning of the GC reaction, and possibly evolves during the reaction, we have

$$[a_i] + 2 \sum_{j=1}^{N_e} [B_j^i] \theta_j^i = [a_i^T]. \quad (9)$$

We solve Eq. (9) for $[a_i]$ iteratively using the Newton-Raphson method. (64)

With θ_j^i determined, we can compute the activation h_j^i . Kepler and Perelson (32) modeled a single lineage and used $h_j^1 = 2\theta_j^1$ with $K_j^{12} = 0$, *i.e.*, they treated all BCRs as monovalent. In the present model, we modified the functional form of h to match the observations of GC size evolution of Wittenbrink et al. (42), while keeping most of the parameters from the KP93 model (32). Specifically, we defined the activation function as

$$h_j^i = \rho(\theta_j^i)^\epsilon \quad (10)$$

and performed least squares optimization to improve agreement with the average GC data (42), to obtain $\rho = 0.94$ and $\epsilon = 0.7$ (see Supplementary Material S4 & Fig. S9). Because $\theta_j^i < 1$, the prefactor reduces the activation upper bound to ρ ; the exponent $\epsilon < 1$ increases activation for smaller binding fraction values, reducing the competitive advantage of higher affinity BCRs.

Two comments on Eq. (2) are necessary. First, the proliferation is split into two terms (32) to expose the fact that mutations in a cell of lineage B_j^i during division will lead to the loss of the parent cell and a gain of two daughter cells. Second, the proliferation is not *activated* (*i.e.* not proportional to h_j^i). Whether activation by Ag and T-cells mainly rescues B-cells from apoptosis (death rate proportional to $[1-h]$), (65, 36) or actually increases the rates of proliferation (growth rate proportional to h) has been a matter of some debate, with more recent evidence in favor of activated proliferation. (66) In this study, however, parametrizing the model with activated proliferation would not change the main conclusions; the main difference in the activated proliferation model parameters was that the rate constants k_p^{max} and k_d had to be increased and reduced, respectively, to fit experimental data (see Supplementary Material S5). The fact that in the *nonactivated* proliferation model the B-cell death rate constant is higher than the proliferation rate (Table 1) reflects the importance of rescue from apoptosis to B-cell survival for this model. Comparison of the activated proliferation model results to the experiments (42, 44) is given in Figs. S10 and S11. A study of the two types of proliferation models was performed by Amitai et al. (67), whose main finding was that activated proliferation reduces clonal diversity.

4.0.2 Avidity of simulated BCRs

To examine the effect of BCR avidity on the evolution of B cells within the GC, we compare the behavior of lineages with three regimes of bivalency, corresponding to $K_{eq}^2=0$, $K_{eq}^2=K_{eq}^1$, and $K_{eq}^2=10K_{eq}^1$, which we denote, respectively, as the monovalent, noncooperative, and cooperative binding cases. We can rationalize the chosen values as follows. The binding constant can be expressed in terms of the free energy difference (ΔF) between reactants and products, which is approximately decomposable into rotational, translational (equivalently, concentration) and configurational components(68); Because the two binding arms (Fabs) are identical, we assume that they populate identical conformational ensembles, and therefore their ΔF of binding can only differ in the rotational and translational entropies, and, possibly, in the energetic strain needed to move the second Fab into its binding position. The translational entropy penalty of binding of the second Fab (Fab2) will generally be much smaller than that of the first (Fab1), because the volume accessible to unbound Fab2 is restricted by the binding of Fab1 to its epitope, whereas the volume accessible to an unbound BCR is of the order of the GC volume. More specifically, we can estimate the volume available to Fab2 when Fab1 is bound to be the volume occupied by an antibody, which is of the order $(10nm)^3 = 10^{-24}m^3$. The effective AG concentration is inversely proportional to this volume (*i.e.* we assume that one antigenic site is available to Fab2, restrained by Fab1). In contrast, when Fab1 is unbound, we take the AG concentration to be inversely proportional to the volume of the GC light zone, approximated as 50% of the GC volume ($= 0.5 \times [80\mu m]^3 = 2.56 \times 10^{-13}m^3$) and proportional to the number of individual Ags presented on FDCs. Because antigen is generally abundant in GCs,(69) we take the number of Ags available to bind BCRs as 1000 times the typical B-cell count in a maturing GC, which is around 2000 from Fig. 3. The ratio of antigen concentrations for bound *vs.* unbound Fab1 is then $10^{24} \times 2.56 \times 10^{-13} / (1000 \times 2000) \simeq 10^5$. The difference in the rotational entropy penalty due to binding is expected to be much smaller, because antibodies appear to be sufficiently flexible to permit considerable independent rotation of the individual Fabs.(70) In particular, we expect the difference to be less than an order of magnitude, and neglect this contribution. If energetic strain (*i.e.* ΔE) is needed to accommodate binding of Fab2, it will reduce the binding affinity by the factor $\exp(\Delta E/[k_B T])$. In the absence of experimental data, we assume a strain energy in the range 1-5 kcal/mol, which corresponds to the reduction of K_{eq}^2 by a factor in the range $\exp(1/[k_B T]) - \exp(5/[k_B T]) \simeq 5-4160$, where $k_B T \simeq 0.6$ at $T=300K$. The above crude estimates suggest that, even with a substantial antibody strain of 5kcal/mol, a bivalency binding advantage of $\times 25$ would be present. For simplicity, and to include a margin of safety in our results, we assume a slightly lower binding advantage factor of 10, *i.e.* $K_{eq}^2=10K_{eq}^1$. We also include the monovalent case, $K_{eq}^2 = 0$, which can also be interpreted as requiring infinite strain energy for Fab2 binding, and an intermediate case $K_{eq}^2=K_{eq}^1$, which we label noncooperative.

A possibility that is beyond the scope of this work is to compute strain energy from molecular dynamics simulations of bivalent Ab/Ag binding. However, such simulations are expected to be difficult because of the large sizes of the antibody and antigen molecules involved.

4.0.3 Memory cell production

The basic AM model, Eq. (2), follows the populations of B-cell lineages (*i*) with different affinities (*j*). However, we are also interested in the memory B-cell (MBC) populations produced by different lineages, since these MBCs will be activated in the host upon repeat infections. As in our earlier modeling work,(17) we assume that some of the B-cells exit the GC reaction as MBCs or plasma cells (PCs). MBCs are discussed here and PCs, in the next subsection.

Using M_j^i to denote MBCs of lineage i and affinity j , the corresponding evolution equation is

$$\frac{d[M_j^i]}{dt} = C_M h_j^i (1 - h_j^i) [B_j^i] - k_d^M [M_j^i], \quad (11)$$

where the first term corresponds to differentiation from GC B-cells, and the second, to apoptosis. The fraction $h_j^i(1 - h_j^i)$ preferentially selects B-cells of intermediate affinity, reflecting the observation that higher-affinity B-cells are more likely to recycle into the dark zone, rather than exit as MBCs.(71) The value of C_M is 0.3 (discussed further later) and the death rate constant k_d^M is 0.02/day(72).

4.0.4 Plasma cell and antibody production

Under the assumption of constant Ag concentration, Eqs. (2) converge to a steady-state solution, in which the GC is composed of highest-affinity B-cells, surviving indefinitely.(32) However, it is known that GCs shrink to 5% of their maximum size after about a month.(73) While the assumption of constant antigen used in Ref. 32 is likely to be unrealistic, Ag consumption in the GC is not the main cause of GC shrinkage. It is known that immune complexes presented by follicular dendritic (and other) cells(39) persist for very long times, which is probably necessary for immune memory maintenance.(74)

To account for Ag consumption, we follow Rundell et al. (72) and model it by exponential decay,

$$\frac{d[a_i^T]}{dt} = -k_d^a [a_i^T], \quad (12)$$

with $k_d^a=0.011/\text{day}$, which corresponds to a half life of about 63 days.

To model GC shrinkage consistently with the experimental observations of GC size,(42) we adopt the antibody feedback model of Zhang et al. (31). The essential concept is that some of the maturing B-cells differentiate into PCs, which secrete Abs. These Abs can diffuse throughout the GCs and compete with BCRs for antigen. Once the Abs are sufficiently numerous and of high affinity, the GC shrinks. Although the process of GC shrinkage is probably considerably more complicated, involving regulatory T cells and various signaling molecules, we employ the Ab feedback model here because it requires few additional variables and parameters (see below), and is able to capture GC size evolution over time, as shown here and in Ref. 31.

Since antibodies are secreted by PCs, we began with the PC evolution equation

$$\frac{d[P_j^i]}{dt} = C_P h_j^i (1 - h_j^i) [B_j^i] - k_d^P [P_j^i]. \quad (13)$$

However, our attempts at fitting this model to the PC production data of Weisel et al. (44) did not yield good agreement. The main reason is that the MBC and PC production rates have different evolution profiles in the experiments (see Fig. 3B vs. Fig. 3C), with the MBC rate decreasing rapidly, while the PC rate remains essentially constant within the experimental uncertainty. In contrast, our models for the two quantities (Eqs. (11) and (13)) are the same, except for the numerical values of the parameters. To improve agreement in the PC rate, we added an additional, semiempirical, source term to Eq. (13), $k_M^P [M_j^i]$, to mimic low-level differentiation of MBCs activated by immune complexes carrying antigen into late

619 B-blasts, which differentiate into long-lived PCs.(75, 72) The resulting PC evolution equation is

$$\frac{d[P_j^i]}{dt} = C_P h_j^i (1 - h_j^i) [B_j^i] + k_M^P [M_j^i] - k_d^P [P_j^i], \quad (14)$$

620 which maintains some PC production even if the B-cell (but not MBC) population vanishes.

621 In Eq. (14) the value of the death rate constant k_d^P is 0.0336/day(72), the differentiation constant C_P is 0.7,
 622 and the production constant k_M^P is 0.18/day. C_P and k_M^P were first set by trial and error and subsequently
 623 refined by least squares fitting to reproduce the average GC dynamics. While we could not obtain a
 624 biologically-motivated value for k_M^P , we note that it is about an order of magnitude lower than the B-cell
 625 proliferation constant (see Table 1), consistent with its role as a lesser source of PCs. However, its value
 626 still appears to be unphysically high, especially in comparison to the MBC death rate of 0.02/d (Eq. (11)),
 627 possibly reflecting deficiencies or oversimplifications in the differentiation components of the model. For
 628 example, the probabilities of a B-cell exiting the GC to differentiate into an MBC vs. a PC are kept constant
 629 ($C_M=0.3$ vs. $C_P=0.7$). Recent data suggests that PCs tend to be produced more frequently in later stages of
 630 the GC reaction,(44) and that a PC is more likely to result than an MBC if the B-cell has higher affinity for
 631 antigen, and/or receives more T-cell help.(71) However, because quantitative data describing the relative
 632 MBC/PC output is scarce and imprecise, we do not implement an affinity dependence in the MBC/PC
 633 differentiation choice, and instead use the same preference for B-cells of intermediate affinity in both cases
 634 via the factor $h_j^i(1 - h_j^i)$ in Eqs. (11) and (14). More sophisticated affinity-based cell fate decisions are
 635 probably needed in these equations. They can be modeled using other functions of h_j^i , or by introducing
 636 other biological species or signaling molecules, as more precise data become available.

637 Antibodies are secreted by PCs and their removal is modeled with exponential decay

$$\frac{d[A_j^i]}{dt} = k_p^A [P_j^i] - k_d^A [A_j^i]. \quad (15)$$

638 The Ab death rate constant k_d^A is obtained from the half-life of 10d,(31) and an approximate secretion k_p^A
 639 rate constant is obtained as follows. We assume that every PC secretes 1.7×10^8 Ab molecules/day(76).
 640 However, the Abs are allowed to diffuse freely in and out of GCs, and, assuming that the diffusion
 641 is fast enough to establish equilibrium, we scale this rate by the ratio of internal to external volumes
 642 corresponding to a single GC. The internal volume is taken as the volume of a sphere of radius $80\mu m$,(42)
 643 and the external volume is taken to be $0.04mL$ (31), which gives $k_p^A=8500/day$. Starting from this value, and
 644 the PC differentiation parameter $C_P=0.5$, we used least squares fitting to improve the agreement between
 645 the model and the average GC sizes of Wittenbrink et al. (42) (an example of parameter fitting is shown in
 646 Supplementary Material S4). The optimized values were $k_p^A=35000/day$ and $C_P=0.7$, corresponding to
 647 higher values of Ab production needed to achieve faster GC shrinkage.

648 The effect of Ab competition is incorporated by modifying the Ag conservation Eq. (9) to include binding
 649 to Abs,

$$\begin{aligned} [a_i] + 2 \sum_{j=1}^{N_\epsilon} ([A_j^i/\sigma] + [B_j^i]) \theta_j^i = \\ [a_i] + \sum_{j=1}^{N_\epsilon} [C_j^i] \theta_j^i = [a_i^T], \end{aligned} \quad (16)$$

where we assumed that Abs bind antigen in the same manner as do BCRs, and defined a total receptor concentration $[C_j^i] \equiv 2([A_j^i/\sigma] + [B_j^i])$; the scaling factor $\sigma = 10^5$ appears because each B-cell (B_j^i) is assumed to have 10^5 BCRs,(62) which have the same binding valency as Abs.

At this stage, the model, as written in Eq. (2), does not have explicit limitations on the maximum GC size. The shape of the B-cell population curve is governed entirely by proliferation, death and competition with Abs. To obtain a close match to the peak in the experimental B-cell count,(42) we follow others (33, 72) and introduce a maximum lineage size $B_{max} = 5000$ cells. The proliferation rate is modified as follows,

$$k_p = k_p^{max} \times \left(1 - \frac{\sum_j [B_j]}{B_{max}}\right), \quad (17)$$

where k_p^{max} is the maximum proliferation rate. A similar idea was used by Amitai et al. (24), who increased the cell death rate, as a critical B-cell population was approached.

4.0.5 Clonal competition via epitope occlusion

Thus far, we have described a model which has competition only within each clonal lineage, *i.e.*, higher-affinity cells outcompete lower-affinity cells, and are themselves eventually outcompeted by growing numbers of high-affinity Abs derived from them. However, GCs are seeded by multiple lineages, and it is therefore important to consider the effects of interclonal competition. In the context of influenza, it would be of interest to model how anti-HA-head Abs could directly compete with anti-HA-stem Abs.

Toward this end, we generalize the model by introducing a distinction between epitopes and antigens. Specifically, we recognize that a single antigen can present different epitopes. For example, an entire viral spike may be considered an antigen with many different epitopes, each targeted by a different activated B cell. We postulate that the binding of a BCR or Ab of type k to its cognate epitope a_k can reduce the accessibility of epitope a_i , so that the effective concentration of a_i available to bind is reduced by a fraction of the bound concentration of a_k . We label this reduction $\Delta^k[a_i]$, which is

$$\Delta^k[a_i] = -O_{ik} \sum_{j=1}^{N_\epsilon} [C_j^k] \theta_j^k, \quad \text{with } 0 \leq O_{ik} \leq 1, \quad i \neq j, \quad (18)$$

where we introduced the *occlusion* tensor O_{ik} , which models the effect of epitope k occupancy on epitope i . In particular, $O_{ik}=0$ corresponds to the absence of interaction, and $O_{ik}=1$ implies that binding of a_k completely prevents binding to a_i (full occlusion). Setting $O_{ii} \equiv 1$, we write the modified Ag conservation equations as

$$[a_i] + \sum_{j=1}^{N_\epsilon} \sum_{k=1}^{N_B} O_{ik} [C_j^k] \theta_j^k = [a_i^T], \quad (19)$$

in which the concentrations $[a_i]$ are now coupled *via* the occlusion tensor (unlike in Eq. (16), in which they are independent). The components of O can in principle be set independently, provided that care is taken to avoid component values so large that negative concentrations could result. For simplicity, we begin with a constant occlusion independent of the antigen identity, *i.e.*, $O_{ik} = o$, for $0 \leq o \leq 1$, and $i \neq k$, and reduce its value to prevent negative AG concentrations. Specifically, if $[a_k^T] > [a_i^T]$ we set

$$O_{ik} = o \times \min \left\{ 1, \frac{[a_i^T]}{[a_k^T]} \right\}. \quad (20)$$

In the simplified case of two BCR/epitope pairs, Eq. (20) can be justified as follows. We combine the conservation equations,

$$\begin{aligned} [a_1] + \sum_{j=1}^{N_\epsilon} [C_j^1] \theta_j^1 + O_{12} [C_j^2] \theta_j^2 &= [a_1^T], \\ [a_2] + \sum_{j=1}^{N_\epsilon} [C_j^2] \theta_j^2 + O_{21} [C_j^1] \theta_j^1 &= [a_2^T] \end{aligned} \quad (21)$$

to obtain

$$[a_1] + (1 - O_{12}O_{21}) \sum_{j=1}^{N_\epsilon} [C_j^1] \theta_j^1 = [a_1^T] - O_{12}([a_2^T] - [a_2]). \quad (22)$$

Because $1 - O_{12}O_{21} \geq 0$ and the bound fraction θ^1 is zero only if $[a_1] = 0$ (we assume that the binding constants are not both zero), to ensure $[a_1] \geq 0$, it is sufficient to require

$$[a_1^T] - O_{12}([a_2^T] - [a_2]) \geq 0, \quad (23)$$

or

$$O_{12} \leq \frac{[a_1^T]}{[a_2^T] - [a_2]}. \quad (24)$$

Eq. (20) satisfies this condition, since we also assume that $[a_2]$ is nonnegative.

We note that the occlusion tensor is similar in spirit to the interaction matrix used by Yan and Wang (45). However, as these authors had a different purpose, specifically, to model synergistic vs. antagonistic effects of Abs derived from previous B cell lineages on B cells in the current generation, they allowed negative interference values, which are not physically justifiable in our model, as they would imply creation of Ag.

4.0.6 Integration of model equations

In this section we describe the numerical procedures used to compute the time-dependent concentrations of the Ags, cells, and Abs in the GC. First, following Kepler and Perelson (32), we make all concentrations nondimensional using the total concentration of one of the antigens at the beginning of simulation. For single-epitope (validation) simulations, we use the sole epitope. For multi-epitope simulations, we arbitrarily elected to use the second epitope, to be able to vary the concentrations of the first epitope for studying the effects of epitope concentration in maturation. Thus, the nondimensional variables are $\alpha_i \equiv [a_i]/[a_2^T]$, $x_j^i \equiv [B_j^i]/[a_2^T]$, $y_j^i \equiv [A_j^i]/[a_2^T]$, $p_j^i \equiv [P_j^i]/[a_2^T]$, $w_j^i \equiv [M_j^i]/[a_2^T]$, and $\kappa_j^{ik} = K_j^{ik}/[a_2^T]$.

In the new variables, the nondimensional evolution equations are

$$\frac{dx_j^i}{dt} = \{-k_d(1 - h_j^i) - k_p\} x_j^i + 2k_p \sum_{k=1}^{N_\epsilon} m_{kj} x_k^i, \quad (25)$$

$$\frac{dw_j^i}{dt} = C_M h_j^i (1 - h_j^i) x_j^i - k_d^M w_j^i, \quad (26)$$

$$\frac{dp_j^i}{dt} = C_P h_j^i (1 - h_j^i) x_j^i + k_M^P w_j^i - k_d^P x_j^i, \quad (27)$$

$$\frac{dy_j^i}{dt} = k_p^A p_j^i - k_d^A y_j^i, \quad (28)$$

$$\frac{d\alpha_i^T}{dt} = -k_d^A \alpha_i^T, \quad \text{for } 1 \leq i \leq N_B, 1 \leq j \leq N_\epsilon. \quad (29)$$

and the nondimensional AG conservation equations are

$$\alpha_i + 2 \sum_{j=1}^{N_\epsilon} \sum_{k=1}^{N_B} O_{ik} (x_j^k + \sigma^{-1} y_j^k) \theta_j^k = \alpha_i^T, \quad (30)$$

$$\theta_j^i = \frac{1}{2} \cdot \frac{\kappa_j^{i1} x_j^i (1 + 2\kappa_j^{i2} x_j^i)}{1 + \kappa_j^{i1} x_j^i (1 + \kappa_j^{i2} x_j^i)}, \quad (31)$$

$$O_{ik} = o \times \min \left\{ 1, \frac{\alpha_i^T}{\alpha_k^T} \right\}, \quad (32)$$

and the expressions for m_{ij} and h are the unchanged.

We follow Kepler and Perelson (32) and take the dimensionless affinities $\kappa^{min} = 7.5^{-2}$, $\kappa^{max} = 7.5^5$, but use $N_\epsilon=20$ affinity bins, compared to their 8, for a finer discretization. This corresponds to $\Delta E \simeq 0.74$ in Eq. (1). Eq. (25) – Eq. (29) were integrated in Octave(77) using the explicit Euler method,(78) with the time step $dt = 0.01 \times \text{day}$. At each iteration, Eq. (30) was solved for α_i using the iterative Newton-Raphson (NR) method(64). The initial guess at the current iteration was taken as the corresponding value in the previous iteration, which ensured that convergence required only a few NR iterations. At the beginning of the simulation, the initial guesses were $\alpha_i = \alpha_i^T$. Simulation duration was 35 days, requiring less than a minute of computer time using a single computing node with an Intel Xeon E5 2.3 GHz Haswell CPU. However, the simulation cost was approximately linearly dependent on the number of BCR/Ag pairs simulated. The simulation parameters and their values are listed in Table 1.

4.0.7 Initial conditions

Initial values correspond to time $t=0$. For single-epitope simulations $\alpha_1^T=1$. For multi-epitope simulations, $\alpha_2^T=1$, by definition of the normalization and $\alpha_i^T=1$ for $i > 2$. The concentration of the first epitope α_1^T was varied between 1 and 2, depending on simulation to investigate the effects of AG concentration (see Results). The initial population of each B-cell lineage was 100 cells, because we assumed that a mutation-free expansion of each seeding B-cell has already taken place prior to simulation. The initial distribution of naive B-cell binding constants was log-normal; specifically, we used a Gaussian in the energy space, centered on the 7th class ($\kappa \simeq 1.53$) with standard deviation $\sigma=0.6 \times \Lambda$. This choice was

Table 1. Model and Simulation Parameters. Time is measured in days.

† Used only for computing cell counts *a posteriori*, *i.e.* does not impact simulations;

‡ The affinity bounds apply only to the first binding constant κ_j^{i1} ; the second binding constant was defined as different multiples of the first to investigate avidity effects (see Sec. 2);

* The ratio of advantageous to deleterious but nonlethal mutations is given by $1/(1 + \Lambda^2)$; It is computed by logarithmic scaling of the value $\Lambda^0=30$ of Kepler and Perelson (32) as $\log \Lambda = \Delta E \log \Lambda^0 / \log 7.5$, which accounts for the difference that Kepler and Perelson (32) used an 8-point discretization, or 8 affinity classes (corresponding to $\Delta E = \log 7.5$), while we use 20 classes.

Parameter	Description	Value	Source
k_p^{max}	maximum B-cell proliferation rate	2.2	adjusted from 4(Ref. 32) to fit data(42)
B_{max}	Maximum allowed B-cell count	5000	fit to data(42)
k_d	B-cell death rate	4.125	adjusted from 4(32) to fit data(42)
μ	BCR mutation rate	0.1	Oprea and Perelson (33)
σ	BCRs per B-cell	10^5	Casten and Pierce (62)
p_L	Fraction of lethal mutations	0.5	Kepler and Perelson (32)
C_M	MBC differentiation constant	0.3	fit to data(42, 44)
C_P	PC differentiation constant	0.7	fit to data(42, 44)
k_d^M	MBC death rate	0.02	Rundell et al. (72)
k_d^a	Decay of AG presented to BCRs	0.111	Rundell et al. (72)
k_d^P	PC death rate	0.0336	Rundell et al. (72)
k_M^P	PC production rate from MBCs	0.17	fit to data(44)
k_p^A	AB secretion from PCs	35000	based on Refs 76, 31 (see text)
k_d^A	AB death rate	0.069	Zhang et al. (31)
k_d^a	AG removal rate	0.011	Rundell et al. (72)
ρ	activation prefactor in $h = \rho\theta^\epsilon$	0.94	fit to data(42, 44)
ϵ	activation exponent in $h = \rho\theta^\epsilon$	0.7	fit to data(42, 44)
ξ	Concentration corresponding to one cell†	1e-4	Kepler and Perelson (32)
κ^{min}	Smallest (nondimensional) affinity‡	7.5^{-2}	Kepler and Perelson (32)
κ^{max}	Largest (nondimensional) affinity‡	7.5^5	Kepler and Perelson (32)
Λ	Mutation distribution constant*	$\simeq 3.5$	based on Ref. (32)
N_ϵ	Number of affinity classes	20	up from 8(Ref. 32) for higher resolution

made to approximate by a smooth function the discrete Dirac mass of $\kappa=7.5$, used by Kepler and Perelson (32). The distribution is shown in Fig. 6D of the Results. The above distribution appears to us to be more physical than the sharply peaked distribution of Kepler and Perelson (32). However, we note that we could also obtain a satisfactory fit to the experimental data using the latter distribution, albeit with small parameter adjustments that affect the total GC size and time to GC peak.

For simulations whose purpose was to investigate the effect of an initial affinity advantage on the rate of B-cell proliferation (see Sec. 2), the initial distribution was shifted by scaling the abscissa by a prescribed advantage (ΔK_{eq}), and linearly reinterpolated onto the initial grid in energy space (see Results and Fig. 6D). All initial distributions (of each lineage) were normalized to 100 B-cells.

CONFLICT OF INTEREST STATEMENT

The authors declare that the research was conducted in the absence of any commercial or financial relationships that could be construed as a potential conflict of interest.

AUTHOR CONTRIBUTIONS

730 VO conceived the research; VO performed the simulations; VO and MK analyzed results and wrote the
731 paper.

FUNDING

732 Financial support for this project was provided by the Bill & Melinda Gates Foundation and Flu Lab under
733 grant opportunity OPP1214161. The findings and conclusions contained within are those of the authors
734 and do not necessarily reflect positions or policies of the Bill & Melinda Gates Foundation.

ACKNOWLEDGMENTS

735 The authors are grateful to Drs. Simone Conti and Aravinda Munasinghe for helpful discussions. Computer
736 resources were provided by National Energy Resource Scientific Computing Center (NERSC), which
737 is supported by the Office of Science of the U.S. Department of Energy under Contract No. DE-AC02-
738 05CH11231, and by Oak Ridge Leadership Computing Facility, which is a DOE Office of Science User
739 Facility supported under Contract DE-AC05-00OR22725. Release Number LLNL-JRNL-793877.

SUPPLEMENTAL DATA

740 Supplementary Material accompanies this article, including text appendices S1–S6 and figures S1–S13.
741 The computer code to reproduce the simulation data and figures in this paper can be found online at
742 <https://github.com/ovchinnv/affinity-maturation-paper2021.git>

REFERENCES

- 743 1 .Taubenberger J, Kash J, Morens D. the 1918 Influenza Pandemic: 100 Years of Questions Answered
744 and Unanswered. *Sci. Trans. Med.* **11** (2019) 0. doi:10.1126/scitranslmed.aau5485.
- 745 2 .Andersen K, Rambaut A, Lipkin W, Holmes E, Garry R. the Proximal Origin of SARS-CoV-2. *Nat.*
746 *Med.* **26** (2020) 450–452. doi:10.1038/s41591-020-0820-9.
- 747 3 .Bao Y, Bolotov P, Dernovoy D, Kiryutin B, Zaslavsky L, Tatusova T, et al. The Influenza Virus
748 Resource at the National Center for Biotechnology Information. *J. Virol.* **82** (2008) 596–601. doi:10.
749 1128/JVI.02005-07.
- 750 4 .MATLAB. *Version 7.10.0 (R2010a)* (Natick, Massachusetts: The MathWorks Inc.) (2010).
- 751 5 .Xu R, Ekiert D, Krause J, Hai R, Crowe J, Wilson I. Structural Basis of Preexisting Immunity to the
752 2009 H1N1 Pandemic Influenza Virus. *Science* **328** (2010) 357–60. doi:10.1126/science.1186430.
- 753 6 .Humphrey W, Dalke A, Schulten K. VMD - Visual Molecular Dynamics. *J. Mol. Graphics* **14** (1996)
754 33–38.
- 755 7 .Nachbagauer R, Choi A, Hirsh A, Margine I, Iida S, Barrera A, et al. Defining the Antibody Cross-
756 Reactome Directed Against the Influenza Virus Surface Glycoproteins. *Nat. Immunol.* **18** (2017)
757 464–473. doi:10.1038/ni.3684.
- 758 8 .Corti D, Cameroni E, Guarino B, Kallewaard N, Zhu Q, Lanzavecchia A. Tackling Influenza with
759 Broadly Neutralizing Antibodies. *Curr. Opin. Virol.* **24** (2017) 60–69. doi:10.1016/j.coviro.2017.03.
760 002.

- 761 **9** .Watanabe A, McCarthy K, Kuraoka M, Schmidt A, Adachi Y, Onodera T, et al. Antibodies to a
762 Conserved Influenza Head Interface Epitope Protect by an IgG Subtype-Dependent Mechanism. *Cell*
763 **177** (2019) 1124–1135.e16. doi:10.1016/j.cell.2019.03.048.
- 764 **10** .Bajic G, Maron M, Adachi Y, Onodera T, McCarthy K, McGee C, et al. Influenza Antigen Engineering
765 Focuses Immune Responses to a Subdominant but Broadly Protective Viral Epitope. *Cell host &*
766 *microbe* **25** (2019) 827–835.e6. doi:10.1016/j.chom.2019.04.003.
- 767 **11** .Raymond D, Bajic G, Ferdman J, Suphaphiphat P, Settembre E, Moody M, et al. Conserved Epitope
768 on Influenza-Virus Hemagglutinin Head Defined by a Vaccine-Induced Antibody. *Proc. Natl. Acad.*
769 *Sci. USA* **115** (2018) 168–173. doi:10.1073/pnas.1715471115.
- 770 **12** .Bajic G, van der Poel C, Kuraoka M, Schmidt A, Carroll M, Kelsoe G, et al. Autoreactivity Profiles of
771 Influenza Hemagglutinin Broadly Neutralizing antibodies. *Sci. Rep.* **9** (2019) 3492. doi:10.1038/
772 s41598-019-40175-8.
- 773 **13** .Kallewaard N, Corti D, Collins P, Neu U, McAuliffe J, Benjamin E, et al. Structure and Function
774 Analysis of an Antibody Recognizing All Influenza a Subtypes. *Cell* **166** (2016) 596–608. doi:10.
775 1016/j.cell.2016.05.073.
- 776 **14** .Corti D, Voss J, Gamblin S, Codoni G, Macagno A, Jarrossay D, et al. a Neutralizing Antibody Selected
777 from Plasma Cells That Binds to Group 1 and Group 2 Influenza a Hemagglutinins. *Science (New York,*
778 *N.Y.)* **333** (2011) 850–6. doi:10.1126/science.1205669.
- 779 **15** .Li G, Chiu C, Wrammert J, McCausland M, Andrews S, Zheng N, et al. Pandemic H1N1 Influenza
780 Vaccine Induces a Recall Response in Humans That Favors Broadly Cross-Reactive Memory B Cells.
781 *Proc. Natl. Acad. Sci. USA* **109** (2012) 9047–52. doi:10.1073/pnas.1118979109.
- 782 **16** .Prigent J, Jarossay A, Planchais C, Eden C, Dufloo J, Kök A, et al. Conformational plasticity
783 in broadly neutralizing hiv-1 antibodies triggers polyreactivity. *Cell Rep.* **23** (2018) 2568–2581.
784 doi:10.1016/j.celrep.2018.04.101.
- 785 **17** .Ovchinnikov V, Louveau J, Barton J, Karplus M, Chakraborty A. Role of Framework Mutations
786 and Antibody Flexibility in the Evolution of Broadly Neutralizing Antibodies. *eLife* **7** (2018) 0.
787 doi:10.7554/eLife.33038.
- 788 **18** .Ellebedy A, Krammer F, Li G, Miller M, Chiu C, Wrammert J, et al. Induction of Broadly Cross-
789 Reactive Antibody Responses to the Influenza Ha Stem Region Following H5N1 Vaccination in
790 Humans. *Proc. Natl. Acad. Sci. USA* **111** (2014) 13133–8. doi:10.1073/pnas.1414070111.
- 791 **19** .Tan H, Jegaskanda S, Juno J, Esterbauer R, Wong J, Kelly H, et al. Subdominance and Poor Intrinsic
792 Immunogenicity Limit Humoral Immunity Targeting Influenza Ha Stem. *The J. Clin. Invest.* **129** (2019)
793 850–862. doi:10.1172/JCI123366.
- 794 **20** .Arevalo C, Le Sage V, Bolton M, Eilola T, Jones J, Kormuth K, et al. Original Antigenic Sin Priming of
795 Influenza Virus Hemagglutinin Stalk Antibodies. *Proc. Natl. Acad. Sci. USA* **117** (2020) 17221–17227.
796 doi:10.1073/pnas.1920321117.
- 797 **21** .Nachbagauer R, Choi A, Izikson R, Cox M, Palese P, Krammer F. Age Dependence and Isotype
798 Specificity of Influenza Virus Hemagglutinin Stalk-Reactive Antibodies in Humans. *mBio* **7** (2016)
799 e01996–15. doi:10.1128/mBio.01996-15.
- 800 **22** .Andrews S, Huang Y, Kaur K, Popova L, Ho I, Pauli N, et al. Immune History Profoundly Affects
801 Broadly Protective B Cell Responses to Influenza. *Sci. Trans. Med.* **7** (2015) 316ra192. doi:10.1126/
802 scitranslmed.aad0522.
- 803 **23** .Xiao X, Chen W, Feng Y, Zhu Z, Prabakaran P, Wang Y, et al. Germline-like predecessors of broadly
804 neutralizing antibodies lack measurable binding to hiv-1 envelope glycoproteins: implications for

- 805 evasion of immune responses and design of vaccine immunogens. *Biochem. Biophys. Res. Commun.*
 806 **390** (2009) 404–9. doi:10.1016/j.bbrc.2009.09.029.
- 807 **24** .Amitai A, Sangesland M, Barnes R, Rohrer D, Lonberg N, Lingwood D, et al. Defining and
 808 Manipulating B Cell Immunodominance Hierarchies to Elicit Broadly Neutralizing Antibody Responses
 809 Against Influenza Virus. *Cell Syst.* **11** (2020) 573–588.e9. doi:10.1016/j.cels.2020.09.005.
- 810 **25** .Wang S. Optimal Sequential Immunization Can Focus Antibody Responses Against Diversity Loss
 811 and Distraction. *PLoS Comput. Biol.* **13** (2017) 1–27. doi:10.1371/journal.pcbi.1005336.
- 812 **26** .Ives S, Bürckert JP, Pettus C, Peñate K, Hovde R, Bayless N, et al. a General Solution to Broad-Spectrum
 813 Vaccine Design for Rapidly Mutating Viruses. *submitted* (2020). doi:10.21203/rs.3.rs-100459/v1.
- 814 **27** .Harris A, Meyerson J, Matsuoka Y, Kuybeda O, Moran A, Bliss D, et al. Structure and Accessibility
 815 of Ha Trimers on Intact 2009 H1N1 Pandemic Influenza Virus to Stem Region-Specific Neutralizing
 816 Antibodies. *Proc. Natl. Acad. Sci. USA* **110** (2013) 4592–7. doi:10.1073/pnas.1214913110.
- 817 **28** .Kanekiyo M, Joyce M, Gillespie R, Gallagher J, Andrews S, Yassine H, et al. Mosaic Nanoparticle
 818 Display of Diverse Influenza Virus Hemagglutinins Elicits Broad B Cell Responses. *Nat. Immunol.* **20**
 819 (2019) 362–372. doi:10.1038/s41590-018-0305-x.
- 820 **29** .Cohen A, Gnanapragasam P, Lee Y, Hoffman P, Ou S, Kakutani L, et al. Mosaic Nanoparticles Elicit
 821 Cross-Reactive Immune Responses to Zoonotic Coronaviruses in Mice. *Science (New York, N.Y.)* **371**
 822 (2021) 735–741. doi:10.1126/science.abf6840.
- 823 **30** .Williams W, Meyerhoff R, Edwards R, Li H, Manne K, Nicely N, et al. Fab-dimerized glycan-
 824 reactive antibodies are a structural category of natural antibodies. *Cell* **184** (2021) 2955–2972.e25.
 825 doi:10.1016/j.cell.2021.04.042.
- 826 **31** .Zhang Y, Meyer-Hermann M, George L, Figge M, Khan M, Goodall M, et al. Germinal Center B Cells
 827 Govern Their Own Fate Via Antibody Feedback. *J. Exp. Med.* **210** (2013) 457–64. doi:10.1084/jem.
 828 20120150.
- 829 **32** .Kepler T, Perelson A. Somatic Hypermutation in B Cells: An Optimal Control Treatment. *J. Theor.*
 830 *Biol.* **164** (1993) 37–64. doi:10.1006/jtbi.1993.1139.
- 831 **33** .Oprea M, Perelson AS. Somatic Mutation Leads to Efficient Affinity Maturation When Centrocytes
 832 Recycle Back to Centroblasts. *J. Immunol.* **158** (1997) 5155–5162.
- 833 **34** .Meyer-Hermann M. a Mathematical Model for the Germinal Center Morphology and Affinity
 834 Maturation. *J. Theor. Biol.* **216** (2002) 273–300. doi:10.1006/jtbi.2002.2550.
- 835 **35** .Meyer-Hermann M, Mohr E, Pelletier N, Zhang Y, Victora G, Toellner K. a Theory of Germinal Center
 836 B Cell Selection, division, and exit. *Cell Rep.* **2** (2012) 162–74. doi:10.1016/j.celrep.2012.05.010.
- 837 **36** .Zhang J, Shakhnovich E. Optimality of Mutation and Selection in Germinal Centers. *PLoS Comput.*
 838 *Biol.* **6** (2010) e1000800. doi:10.1371/journal.pcbi.1000800.
- 839 **37** .Wang S, Mata-Fink J, Kriegsman B, Hanson M, Irvine D, Eisen H, et al. Manipulating the Selection
 840 Forces During Affinity Maturation to Generate Cross-Reactive HIV Antibodies. *Cell* **160** (2015)
 841 785–797. doi:10.1016/j.cell.2015.01.027.
- 842 **38** .Robert P, Marschall A, Meyer-Hermann M. Induction of Broadly Neutralizing Antibodies in Germinal
 843 Centre Simulations. *Curr. Opin. Biotech.* **51** (2018) 137–145. doi:10.1016/j.copbio.2018.01.006.
- 844 **39** .Allen C, Okada T, Cyster J. Germinal-Center Organization and Cellular Dynamics. *Immunity* **27** (2007)
 845 190–202. doi:10.1016/j.immuni.2007.07.009.
- 846 **40** .Mayer A, Zhang Y, Perelson A, Wingreen N. Regulation of T Cell Expansion by Antigen Presentation
 847 Dynamics. *Proc. Natl. Acad. Sci. USA* **116** (2019) 5914–5919. doi:10.1073/pnas.1812800116.
- 848 **41** .Erwin S, Childs L, Ciupe S. Mathematical model of broadly reactive plasma cell production. *Sci. Rep.*
 849 **10** (2020) 3935. doi:10.1038/s41598-020-60316-8.

- 850 **42** .Wittenbrink N, Klein A, Weiser A, Schuchhardt J, Or-Guil M. Is There a Typical Germinal Center? a
 851 Large-Scale Immunohistological Study on the Cellular Composition of Germinal Centers During the
 852 Hapten-Carrier-Driven Primary Immune Response in Mice. *J. Immunol. (Baltimore, Md. : 1950)* **187**
 853 (2011) 6185–96. doi:10.4049/jimmunol.1101440.
- 854 **43** .Pélissier A, Akrouit Y, Jahn K, Kuipers J, Klein U, Beerenwinkel N, et al. Computational Model
 855 Reveals a Stochastic Mechanism Behind Germinal Center Clonal Bursts. *Cells* **9** (2020) 0. doi:10.
 856 3390/cells9061448.
- 857 **44** .Weisel F, Zuccarino-Catania G, Chikina M, Shlomchik M. a Temporal Switch in the Germinal
 858 Center Determines Differential Output of Memory B and Plasma Cells. *Immunity* **44** (2016) 116–130.
 859 doi:10.1016/j.immuni.2015.12.004.
- 860 **45** .Yan L, Wang S. Shaping Polyclonal Responses via Antigen-Mediated Antibody Interference. *iScience*
 861 **23** (2020) 101568. doi:https://doi.org/10.1016/j.isci.2020.101568.
- 862 **46** .Turner J, Zhou J, Han J, Schmitz A, Rizk A, Alsoussi W, et al. Human germinal centres engage
 863 memory and naive B cells after influenza vaccination. *Nature* **586** (2020) 127–132. doi:10.1038/
 864 s41586-020-2711-0.
- 865 **47** .Nachbagauer R, Liu W, Choi A, Wohlbold T, Atlas T, Rajendran M, et al. a Universal Influenza Virus
 866 Vaccine Candidate Confers Protection Against Pandemic H1N1 Infection in Preclinical Ferret Studies.
 867 *NPJ vaccines* **2** (2017) 26. doi:10.1038/s41541-017-0026-4.
- 868 **48** .Krammer F, Pica N, Hai R, Tan G, Palese P. Hemagglutinin Stalk-Reactive Antibodies Are Boosted
 869 Following Sequential Infection with Seasonal and Pandemic H1N1 Influenza Virus in Mice. *J. Virol.*
 870 **86** (2012) 10302–7. doi:10.1128/JVI.01336-12.
- 871 **49** .Eggink D, Goff P, Palese P. Guiding the Immune Response Against Influenza Virus Hemagglutinin
 872 Toward the Conserved Stalk Domain by Hyperglycosylation of the Globular Head Domain. *J. Virol.* **88**
 873 (2014) 699–704. doi:10.1128/JVI.02608-13.
- 874 **50** .Zhou T, Doria-Rose N, Cheng C, Stewart-Jones G, Chuang G, Chambers M, et al. Quantification
 875 of the Impact of the HIV-1-Glycan Shield on Antibody Elicitation. *Cell Rep.* **19** (2017) 719–732.
 876 doi:10.1016/j.celrep.2017.04.013.
- 877 **51** .Yassine H, Boyington J, McTamney P, Wei C, Kanekiyo M, Kong W, et al. Hemagglutinin-Stem
 878 Nanoparticles Generate Heterosubtypic Influenza Protection. *Nat. Med.* **21** (2015) 1065–70. doi:10.
 879 1038/nm.3927.
- 880 **52** .Corbett K, Moin S, Yassine H, Cagigi A, Kanekiyo M, Boyoglu-Barnum S, et al. Design of
 881 Nanoparticulate Group 2 Influenza Virus Hemagglutinin Stem Antigens That Activate Unmutated
 882 Ancestor B Cell Receptors of Broadly Neutralizing Antibody Lineages. *mBio* **10** (2019) 0.
 883 doi:10.1128/mBio.02810-18.
- 884 **53** .Boyoglu-Barnum S, Hutchinson G, Boyington J, Moin S, Gillespie R, Tsybovsky Y, et al. Glycan
 885 Repositioning of Influenza Hemagglutinin Stem Facilitates the Elicitation of Protective Cross-Group
 886 Antibody Responses. *Nature Commun.* **11** (2020) 791. doi:10.1038/s41467-020-14579-4.
- 887 **54** .Garg A, Mittal S, Padmanabhan P, Desikan R, Dixit N. Increased B Cell Selection Stringency In
 888 Germinal Centers Can Explain Improved COVID-19 Vaccine Efficacies With Low Dose Prime or
 889 Delayed Boost. *Frontiers Immunol.* **12** (2021) 776933. doi:10.3389/fimmu.2021.776933.
- 890 **55** .Galimidi R, Klein J, Politzer M, Bai S, Seaman M, Nussenzweig M, et al. Intra-spike crosslinking
 891 overcomes antibody evasion by HIV-1. *Cell* **160** (2015) 433–46. doi:10.1016/j.cell.2015.01.016.
- 892 **56** .Keating R, Johnson J, Brice D, Labombarde J, Dent A, McGargill M. Broadly Reactive Influenza
 893 Antibodies Are Not Limited by Germinal Center Competition with High-Affinity Antibodies. *mBio* **11**
 894 (2020) 0. doi:10.1128/mBio.01859-20.

- 895 **57** .Barnes C, West A, Huey-Tubman K, Hoffmann M, Sharaf N, Hoffman P, et al. Structures of
 896 Human Antibodies Bound to SARS-CoV-2 Spike Reveal Common Epitopes and Recurrent Features of
 897 Antibodies. *Cell* **182** (2020) 828–842. doi:10.1016/j.cell.2020.06.025.
- 898 **58** .Robert P, Arulraj T, Meyer-Hermann M. Ymir: A 3d structural affinity model for multi-epitope vaccine
 899 simulations. *iScience* **24** (2021) 102979. doi:10.1016/j.isci.2021.102979.
- 900 **59** .Conti S, Kaczorowski K, Song G, Porter K, Andrabi R, Burton D, et al. Design of Immunogens to
 901 Elicit Broadly Neutralizing Antibodies Against HIV Targeting the CD4 Binding Site. *Proc. Natl. Acad.*
 902 *Sci. USA* **118** (2021) 0. doi:10.1073/pnas.2018338118.
- 903 **60** .Sprenger K, Conti S, Ovchinnikov V, Chakraborty A, Karplus M. Multiscale affinity maturation
 904 simulations to elicit broadly neutralizing antibodies against hiv. *submitted, PLoS Comput. Biol.* (2021).
- 905 **61** .Cohen A, Yang Z, Gnanapragasam P, Ou S, Dam K, Wang H, et al. Construction, characterization, and
 906 immunization of nanoparticles that display a diverse array of influenza ha trimers. *PloS one* **16** (2021)
 907 e0247963. doi:10.1371/journal.pone.0247963.
- 908 **62** .Casten L, Pierce S. Receptor-Mediated B Cell Antigen Processing. Increased Antigenicity of a
 909 Globular Protein Covalently Coupled to Antibodies Specific for B Cell Surface Structures. *J. Immunol.*
 910 *(Baltimore, Md. : 1950)* **140** (1988) 404–10.
- 911 **63** .Alberts B, Johnson A, Lewis J, Raf M, Roberts K, Walter P. *Molecular Biology of the Cell* (New York:
 912 Garland Science), fourth edn. (2002).
- 913 **64** .Press W, Flannery B, Teukolsky S, Vetterling W. *Numerical Recipes in FORTRAN 77: The Art of*
 914 *Scientific Computing* (Cambridge University Press), second edn. (1992).
- 915 **65** .Anderson S, Khalil A, Uduman M, Hershberg U, Louzoun Y, Haberman A, et al. Taking Advantage:
 916 High-Affinity B Cells in the Germinal Center Have Lower Death Rates, but similar rates of division,
 917 compared to low-affinity cells. *J. Immunol. (Baltimore, Md. : 1950)* **183** (2009) 7314–25. doi:10.4049/
 918 jimmunol.0902452.
- 919 **66** .Gitlin A, Mayer C, Oliveira T, Shulman Z, Jones M, Koren A, et al. HUMORAL IMMUNITY. T Cell
 920 Help Controls the Speed of the Cell Cycle in Germinal Center B Cells. *Science (New York, N.Y.)* **349**
 921 (2015) 643–6. doi:10.1126/science.aac4919.
- 922 **67** .Amitai A, Mesin L, Victora G, Kardar M, Chakraborty A. a Population Dynamics Model for Clonal
 923 Diversity in a Germinal Center. *Front. Microbiol.* **8** (2017) 1693. doi:10.3389/fmicb.2017.01693.
- 924 **68** .Hill TL. *an Introduction to Statistical Thermodynamics* (New York: Dover) (1986).
- 925 **69** .El Shikh M, El Sayed R, Sukumar S, Szakal A, Tew J. Activation of B Cells by Antigens on Follicular
 926 Dendritic Cells. *Trends. Immunol.* **31** (2010) 205–11. doi:10.1016/j.it.2010.03.002.
- 927 **70** .Saphire E, Parren P, Pantophlet R, Zwick M, Morris G, Rudd P, et al. Crystal Structure of a Neutralizing
 928 Human IGG Against HIV-1: A Template for Vaccine Design. *Science (New York, N.Y.)* **293** (2001)
 929 1155–9. doi:10.1126/science.1061692.
- 930 **71** .Ise W, Kurosaki T. Plasma Cell Differentiation During the Germinal Center Reaction. *Immunol. Rev.*
 931 **288** (2019) 64–74. doi:10.1111/imr.12751.
- 932 **72** .Rundell A, DeCarlo R, HogenEsch H, Doerschuk P. the Humoral Immune Response to Haemophilus
 933 Influenzae Type B: A Mathematical Model Based on T-Zone and Germinal Center B-Cell Dynamics. *J.*
 934 *Theor. Biol.* **194** (1998) 341–81. doi:10.1006/jtbi.1998.0751.
- 935 **73** .Kelsoe G. *in Situ* studies of the germinal center reaction. *Adv. Immunol.* **60** (1995) 267–288.
- 936 **74** .Murphy K. *Janeway's Immunobiology* (New York: Garland Science), eighth edn. (2012).
- 937 **75** .Liu Y, Johnson G, Gordon J, MacLennan I. Germinal Centres in T-Cell-Dependent Antibody Responses.
 938 *Immunol. Today* **13** (1992) 17–21. doi:10.1016/0167-5699(92)90199-H.

- 939 76 .Leanderson T, Källberg E, Gray D. Expansion, selection and mutation of antigen-specific b cells in
 940 germinal centers. *Immunol. Rev.* **126** (1992) 47–61. doi:10.1111/j.1600-065x.1992.tb00630.x.
 941 77 .Eaton JW, Bateman D, Hauberg S, Wehbring R. *GNU Octave Version 4.0.0 Manual: A High-Level*
 942 *Interactive Language for Numerical Computations* (2015).
 943 78 .Moin P. *Fundamentals of Engineering Numerical Analysis* (Cambridge University Press) (2001).

FIGURE CAPTIONS

Figure . 1. Influenza hemagglutinin (HA) spike protein colored by residue conservation. Sequences of avian, swine and human influenza type A spike proteins **spanning the years 1918–2019 and subtypes 1–18** were downloaded from the NIH influenza research database(3); conservation was computed in MATLAB(4) after clustering the sequences to 97% identity and multiple alignment. The HA structure was taken from PDB entry 3LZG(5), and the image was generated using Visual Molecular Dynamics.(6) Only the C_{α} atoms are shown.

Figure . 2. Schematic of the GC model used in this study. (A) Model overview: (1) B-cells are activated upon binding to antigen presented on follicular dendritic cells (FDCs, not explicitly modeled); (1a) in the optional T-cell help model (see text) B-cells are activated when the major histocompatibility complex receptor (MHC2) binds to the T-cell receptor (TCR); B-cell activation rescues B-cells from apoptosis, allowing them to mutate and proliferate; (2) depending on the activation signal, B-cells can differentiate to plasma cells (2a), to memory B-cells (2b), or undergo apoptosis (2c); (3) Plasma cells secrete antibodies (Abs), which also compete with B-cell receptors for antigen (4), which is the essential aspect of the Ab feedback model(31) (see text). (B) Hypothetical modes of antibody binding to influenza spikes; bivalent binding without strain (top) corresponds to cooperative binding by antibody arms; bivalent binding with strain (middle) corresponds to noncooperative binding; monovalent binding (bottom) is assumed to be the dominant mode of binding of anti-HA stem antibodies (see Methods for details).

Figure . 3. Comparison of simulation and experiments. A: Total B-cells, B: Memory B-cell production rate, C: Plasma cell production rate. Experimental data for panel A was generated from the GC cross-sectional areas plotted in Fig. S1B of Ref. 42, and converted to B cell counts as done in Ref. 43; The lower and upper error bars in panel A corresponds to 30% and 70% quantiles, respectively ; experimental data for panels B & C was taken from Fig. 4 of Ref. 43, who obtained raw data from Weisel et al. (44); the error bars in B & C correspond to approximately one SD.

Figure . 4. Effect of antibody valency and epitope occlusion on GC properties. Left column (A–C): noninteracting B-cell case ($o = 0$); Right column (D–F): fully interacting B-cell case ($o = 1$); A,D: Total B cells; B,E: Memory cell production rate; insets: total MBC population at end of simulation; C,F: Average affinity of B-cells and MBCs. For the definition of occlusion o , see Sec. 4.0.5.

Figure . 5. Effect of initial affinity advantage on the growth of monovalent B-cells in the fully interacting B-cell case ($o = 1$). Panels A–C show the same quantities as Fig. 4A–C; The affinity distribution corresponding to BCR#1 was shifted toward higher values relative to BCR#2 and BCR#3 (panel D).

Figure . 6. Fraction of MBC#1 (ζ , defined in the text) at the end of six GC simulations for different initial affinity advantage values vs. total number of BCR/Epitope pairs. A: BCR#1 is cooperatively bivalent ($K_{eq}^{12}=10K_{eq}^{11}$); B: BCR#1 is monovalent ($K_{eq}^{12}=0$).

Figure . 7. Effect of BCR valency and epitope concentration on GC evolution, with $o = 1$ (fully competitive case). Panels A–C show the same quantities as Fig. 4A–C; $\alpha_1^T = 2$, $\alpha_2^T = 1$, $\alpha_3^T = 1$; α^T is the nondimensional AG concentration (see Sec. 4.0.6).

Figure . 8. Fraction of MBC#1 vs. number of sequential GC simulations for different initial affinity advantage values and different AG#1 concentrations, with 10 total BCR/Epitope pairs. A & B: MBC#1 fraction (ζ) at the end of simulations. A: BCR#1 is cooperatively bivalent ($K_{eq}^{12}=10K_{eq}^{11}$); B: BCR#1 is monovalent ($K_{eq}^{12}=0$). The four sets of panels A and B show the effect of increasing occlusion from $o=0$ (no competition) to $o=1$ (full competition).

CONTRIBUTION TO THE FIELD

944 Viral pathogens such as influenza, coronavirus, and HIV remain a high source of global mortality and
945 morbidity, because their rapid rate of mutation presents serious challenges to vaccine design. Many anti-
946 viral vaccines are currently in development, but to be effective against future strains, they must raise
947 host immunity to structurally conserved regions of the virus. Unfortunately, viral adaptation conceals
948 such conserved epitopes from the immune system and guides host immunity towards highly variable,
949 distracting epitopes. Success in developing vaccines against rapidly mutating viruses depends critically on
950 understanding and learning how to overcome this distraction. We have developed and validated a computer
951 model of adaptive immunity, in which we simulate the development of high-affinity antibodies to antigenic
952 epitopes with different properties. We find that the mode of antibody binding to antigens can explain
953 experimental results that show that the immune system is easily directed from certain conserved epitopes
954 toward variable ones. We performed additional simulations to explore the influence of antigen concentration
955 on the competition between different antibodies, and whether raised immunity to conserved (but concealed)
956 epitopes could be long lasting. Our results are expected to inform design of universal vaccines.